Universität Rostock Traditio et Innovatio

LEIBNIZ-INSTITUTE OF ATMOSPHERIC PHYSICS IAP

Small-scale Wave Signatures in Noctilucent Clouds Analyzed by Lidar and Camera

Master Thesis in Physics
by Britta Schäfer

Leibniz-Institute of Atmospheric Physics
at the University of Rostock

Supervisors: Prof. Dr. Franz-Josef Lübken,
Leibniz-Institute of Atmospheric Physics and
Institute of Physics, University of Rostock
Dr. Gerd Baumgarten,
Leibniz-Institute of Atmospheric Physics

Rostock, March 22nd, 2019

Abstract

Noctilucent clouds (NLC) are mesospheric ice clouds occurring in the summer hemisphere at high latitudes and an altitude of about 83 km. This region is the coldest of the earth's atmosphere and is characterized by the presence of breaking gravity waves. The processes involved here lead to a variety of structures and instabilities that become visible in noctilucent clouds and are observed by different instruments. In this thesis high-resolution camera and lidar measurements are combined to give a wide overview of the structures at small scales below the Brunt-Väisälä period of 5 minutes and horizontal scales of a few kilometers. For the first time a large amount of lidar profiles with a temporal resolution of 33 ms is analyzed in detail covering about 1600 hours during the summer from 2011 to 2018. A new categorization for these structures is introduced, a spectral analysis of both image and lidar data is performed and simultaneous observations of the same NLC volume by both instruments are investigated. Wave structures are detected down to scales of 10 seconds and 500 meters and wave periods below 5 minutes are found to be present in more than half of the NLC measurement duration during summer 2014.

Zusammenfassung

Leuchtende Nachtwolken (NLC) sind mesosphärische Eiswolken, die im Sommer in hohen Breiten in ca. 83 km auftreten. Diese Region ist die kälteste der gesamten Erdatmosphäre und geprägt vom Brechen von Schwerewellen. Die beteiligten Prozesse bringen eine Vielzahl von Strukturen und Instabilitäten mit sich, die in leuchtenden Nachtwolken sichtbar sind und von verschiedenen Instrumenten gemessen werden. In dieser Arbeit werden hochaufgelöste Kamera- und Lidarmessungen kombiniert. Sie gibt einen breiten Überblick über Strukturen auf zeitlichen Skalen unterhalb der Brunt-Väisälä-Periode von ca. 5 Minuten und horizontalen Skalen von wenigen Kilometern. Zum ersten Mal wird ein großer Datensatz von etwa 1600 Stunden Lidarmessungen mit einer Zeitauflösung von 33 ms aus den Sommern 2011 bis 2018 detailliert analysiert. Eine neue Kategorisierung für diese Strukturen wird eingeführt, spektrale Analysen werden für Kamera- und Lidardaten durchgeführt und gleichzeitige Beobachtungen desselben NLC-Volumens von beiden Instrumenten werden untersucht. Die Gegenwart von Wellenstrukturen wird auf kleinen Skalen bis zu 10 Sekunden und 500 Metern nachgewiesen. Perioden von unter 5 min werden in mehr als der Hälfte der NLC-Messdauer des Sommers 2014 gefunden.

Contents

Chapter 1

Introduction

Noctilucent clouds (NLC) are not only beautiful phenomena on the northern summer night sky at midlatitudes. Beside their spectacular view, they represent the only cloud species that exists in the middle atmosphere at about 83 km altitude despite the very low water vapor content. In this introductory part, the focus lies on atmospheric structure first and noctilucent clouds afterward. Finally, a motivation for emphasizing small-scale structures in middle atmosphere research is given.

1.1 The Earth's Atmosphere

The gas cover around our planet earth is called atmosphere, derived from the ancient Greek words "atmós" for "mist, haze" and "sphaira" for "ball". Its different layers are separated by temperature maximums and minimums. Processes that are important for daily weather observation and prediction take place in the lowest 8-10 km above the surface that are called troposphere and include nearly all of the total water vapor content of the atmosphere. The names of other layers are in ascending order stratosphere, mesosphere and thermosphere (see Fig. 1.1). Nevertheless, ice particles form at altitudes 80-85 km in summer at polar latitudes. A reason for this is that the climatology shows a reversed seasonal cycle in temperature compared to the surface (see Fig. 1.1). Minimum values in summer are 130 K and below (Lübken 1999). These extremely low temperatures being far away from radiative equilibrium are caused by a global, inter-hemispheric, wave-driven circulation that will be described in 2.2.

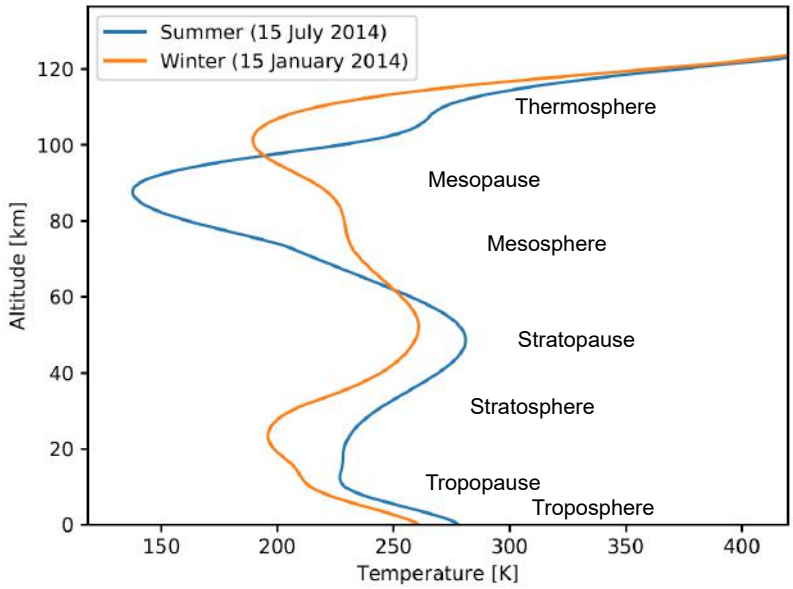

Figure 1.1: Temperature profile of the atmosphere at 69° N, 16° E, summer and winter conditions taken from the MSISE-90 model (Picone et al. 2002)

1.2 Noctilucent Clouds

The first observations of noctilucent clouds were reported in 1885, independently by three scientists in different European countries. These were Otto Jesse in Steglitz (Berlin, Germany), Robert C. Leslie in Southampton (England) and Thomas W. Backhouse in Kissingen (Bavaria, Germany) (Backhouse 1885; Jesse 1885; Leslie 1885). Thus they have been investigated for more than 130 years now and photographs of NLC represent the longest time series of observations from the middle atmosphere. Even though ice particles in the mesosphere might have existed before 1885 it is very likely that the eruption of Krakatoa in 1883 triggered the first observations. Thomas et al. (1989) suppose that the large amount of water vapor ejected into the stratosphere by this event also led to increased diffusion of H_2O into the mesosphere and the growth of ice particles to sizes that are visible from the earth's surface. From the beginning on astronomers and physicists have been interested in the height of these clouds. Only a few years after the discovery it was found to be 82 km on average. In 1896 Jesse published a set of height measurements by triangulation from the years 1889 till 1891 that is not only stunning in its accuracy (82.080 km $\pm$ 0.009 km) but also results in the same value that is today verified by lidar measurements (Fiedler et al. 2017; Jesse 1896). A detailed description of the measurement principles of a lidar will follow later in this thesis in chapter 3.

Noctilucent clouds (from now on short termed NLC) are both interesting in itself, concerning occurrence frequency and spatial spread, and as a tracer to visualize middle atmosphere dynamics. It is still a current object of research to which extent NLC particles can be seen as inert tracers. To be treated such the ice particles must stay invariant in terms of size through relevant time scales. Measurement and model results on formation time, particle size, growth and density are presented by Zasetsky et al. (2009) respectively Kiliani et al. (2013). Maximum particle sizes are about 70 nm. Particles with diameters > 20 nm are big enough to be detected by optical measurement techniques while even smaller particles yield radar echoes called Polar Mesospheric Summer Echoes (PSME) that often occur together with NLC (Nussbaumer et al. 1996). When observed from satellites NLC are called Polar Mesospheric Clouds (PMC) and the most important satellite for research of PMC is the AIM satellite (Aeronomy of Ice in the Mesosphere) with its Cloud Ice Particle Size (CIPS) experiment and Solar Occultation For Ice Experiment (SOFIE) (Russell et al. 2009). NLC reveal a lot of different structures that have been described from camera pictures as morphology types (Fogle and Haurwitz 1966):

I. Veils
   Veils are unstructured clouds, they often appear as a background for other structures.

II. Bands
   Long streaks with either diffuse (II a) or sharply defined edges (II b) are called bands. They are associated with extensive propagating small to medium scale gravity waves, exhibiting horizontal wavelengths of 10 km to >100 km and lifetimes of up to several hours.

III. Billows
   Billows consist of a set of parallel bands. They are subdivided in type III a, short, straight streaks and type III b when exhibiting wave-like structures. They occur spatially limited and are associated with short horizontal wavelengths (5-10 km).

IV. Whirls
   Whirls are complete or partial rings with a dark center. They are classified according to their extent in the spectator's view. A radius of curvature between 0.1° and

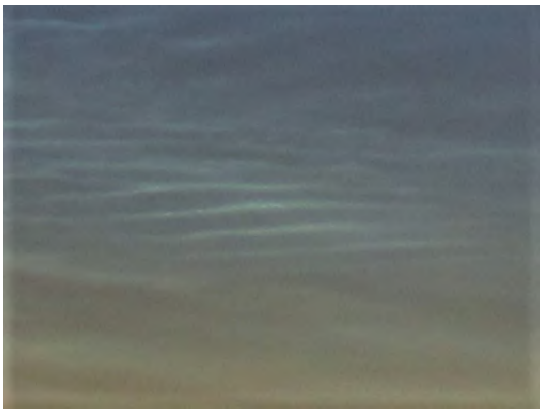

Category I (lower part), III a (middle part),
Trondheim 2015-08-17 00:30:18 UT

Category IV b,
Trondheim 2014-07-23 23:40:03 UT

Category II,
Warnemünde 2015-07-10 21:44:10 UT

Category IV a,
Trondheim 2009-08-01 23:43:20 UT

Figure 1.2: Examples for morphology types of noctilucent clouds as described by Fogle and Haurwitz (1966): The examples were extracted from automated cameras operated by IAP in Trondheim, Norway, and Warnemünde, Germany.

0.5° is considered type IV a, a single bend with curvature between 3° and 5° is assigned type IV b and larger structures are named IV c.

Examples for these types from the IAP NLC camera network are given in Fig. 1.2.

Role of the Middle Atmosphere and NLC in Atmospheric Dynamics and Climate

As motivation it will shortly be discussed why the middle atmosphere and noctilucent clouds are interesting at all in terms of understanding atmospheric dynamics in general,

the earth's climate system or climate change specifically. A recent modeling study by Lübken et al. (2018) contributes to the last question: The water vapor concentration mixing value has increased significantly since the beginning of industrialization due to an increasing methane concentration and thus leads to much brighter NLC. In contrast to that, the increase of CO_2 leading to a warming in the troposphere and a cooling in the middle atmosphere has weaker effects in the mesopause and on the visibility of NLC. Low temperatures are essential but not sufficient for the formation of bright NLC, the availability of water vapor is the limiting factor for the growth of ice particles here. In a more general perspective, the middle atmosphere and lower thermosphere (MLT) is a region where a lot of energy and momentum is dissipated due to the breaking of upward propagating waves transporting energy and momentum upwards from the surface. Most prominent among them are gravity waves (GWs). Their restoring force buoyancy is sensitively dependent on density variations. Along with the decrease of air density when propagating upwards, their amplitudes increase until the waves begin to break and convert to turbulence. Then they create a variety of structures that are observed in NLC by many means: 1) naked eye, 2) camera, 3) lidar profiles, 4) and in-situ measurements on rockets, 5) high-resolution satellite measurements. These small-scale waves are by far too little to be directly resolved in atmospheric circulation models but are represented by parametrizations. In order to get this representation as reliable as possible, it is important to achieve good knowledge about small-scale waves from observations.

In this thesis, both high-resolution lidar and camera measurements are applied in order to understand the appearance and evolution of small scale structures and turbulence in NLC and the mesopause region better. The methods will mostly be interpreted separately, but for a few cases of instantaneous measurements by camera and lidar they will also be brought together. Chapter 2 describes the theoretical background of scattering mechanisms, waves and instabilities in the atmosphere. Chapter 3 introduces the instruments and basic data processing techniques before data analysis follows in chapter 4. This includes among others a new categorization of small-scale features in high-resolution lidar data of NLC and spectral analysis for both camera image and lidar data. Results are presented and discussed in chapter 5 and a summary and outlook will follow in chapter 6.

Chapter 2

Fundamentals

2.1 Scattering Mechanisms in the Atmosphere

The following section is a short repetition of what is important considering the interaction of light and particles in the atmosphere via scattering processes (Kokhanovsky 2001).

The wavelength of a scattered photon depends on the properties of the scattering particle. If the wavelength is equal to the incoming photon, the process is called elastic, if the photon energies are different, the mechanism is inelastic.
Inelastic scattering mechanisms are called rotational and vibrational Raman scattering. Here an electron returns to another rotational or vibrational energy level after scattering. In rotational Raman scattering the wavelength difference is a few nanometers, in vibrational it is tens of nanometers.
Elastic scattering processes are Rayleigh (Cabannes), Aerosol (Mie) and resonance scattering. In elastic mechanisms an electron is lifted to a higher energy level by absorption of the incoming photon. When falling back to the original level a new photon is emitted with the same energy as the absorbed photon. In the case of Cabannes and Mie scattering this higher energy level is a virtual level, in resonance scattering the photon energy corresponds to an atomic transition energy. Therefore the efficiency of the process is higher for the latter (up to five orders). For particles smaller than the wavelength of light Rayleigh scattering dominates, its cross section is strongly

dependent on the wavelength ($\sigma \propto \frac{1}{\lambda^4}$). In this case the scattered intensity is:

$$I = I_0 \left(\frac{1 + \cos^2(\gamma)}{2r^2} \right) \left(\frac{n^2 - 1}{n^2 + 2} \right)^2 \left(\frac{2\pi}{\lambda} \right)^4 \left(\frac{d}{2} \right)^6 \tag{2.1}$$

Here d is the diameter of the particle, n is the refractive index of the scattering material, r is the range between detector and scattering particle, γ is the angle between the incoming and scattered photon and I_0 is the emitted intensity.

For bigger particles with size of the order of the wavelength λ such as aerosols Mie scattering becomes important. The Rayleigh formula given in 2.1 is the small-particle limit in the Mie theory. The first formulation of Mie theory was done for spherical particles, later on also exact solutions for cylinders were developed, but for complicated particle shapes approximations are necessary. For noctilucent clouds the T matrix method and the Discrete Dipole Approximation (DDA) are common techniques. When particles get big compared to λ the Mie solution converges to geometrical optics.

2.2 Atmospheric Waves and Instabilities

Atmospheric dynamics are driven by the difference in the solar power received at the tropics compared to the poles. A circulation system composed of cells transports energy from low to high latitudes. Many different wave phenomena take place in this system, e.g. Rossby waves on planetary scales with the Coriolis force as restoring force, tides excited by day-night periodicity and internal gravity waves with buoyancy as restoring force and scales down to a few kilometers.

Fluid instabilities occur in the atmosphere in many different shapes. First of all, one can distinguish between hydrostatic and hydrodynamic instabilities. An example for the first case are convective instabilities, e.g. a rising air parcel in an unstable stratified atmosphere. Among the second are Kelvin-Helmholtz instabilities (KHI) that appear in the presence of density stratification and a linear shear flow profile.

Gravity Waves

Gravity waves are disturbances in a fluid driven by buoyancy/density gradients as restoring force. After an initial vertical displacement an air parcel in a stably stratified atmosphere starts to oscillate around its equilibrium position. Associated to this movement is the Brunt-Väisälä frequency given by

$$N^2 = \frac{g}{T}\left(\frac{dT}{dz} - \Gamma\right)$$

where Γ (~ -10 K/km) is the adiabatic lapse rate and $\frac{dT}{dz}$ is the temperature gradient of the ambient air. If $\Gamma > \frac{dT}{dz}$ the conditions are statically unstable. The dispersion relation for gravity waves is given by

$$\omega_I^2 = \frac{N^2(k^2+l^2) + f^2\left(m^2 + \frac{1}{4H^2}\right)}{k^2 + l^2 + m^2 + \frac{1}{4H^2}}$$

with f being the Coriolis frequency, H being the scale height and k, l and m being the zonal, meridional and vertical wavenumbers. In another formulation for the vertical wavenumber m (equation 2.2) it becomes obvious that the intrinsic frequencies for propagating waves must range between $|f|$ and N.

$$m^2 = \frac{(k^2+l^2)\,(N^2-\omega_I^2)}{\omega_I^2 - f^2} - \frac{1}{4H^2} \tag{2.2}$$

The upward propagation of gravity waves is restricted by winds. In order to be able to propagate upwards the wind speed must be lower than the phase speed of the wave, otherwise the wave is filtered. The mean wind patterns in summer and winter are shown in Fig. 2.1. It follows that only eastward propagating waves can make it to the mesosphere in the summer hemisphere. Due to the deflection by the Coriolis force this eastward acceleration of air masses is turned into a meridional motion towards the equator. On the winter hemisphere the same procedure leads to a poleward transport stimulated by westward propagating waves. So a meridional circulation is introduced that connects the air masses interhemispherically and transports air from the summer to the winter pole. As required by the continuity of mass, air masses start rising at the summer pole and by cooling down adiabatically they cause the low temperatures in the summer mesopause. On the opposite side downwelling at the winter pole causes a warming of the mesopause.

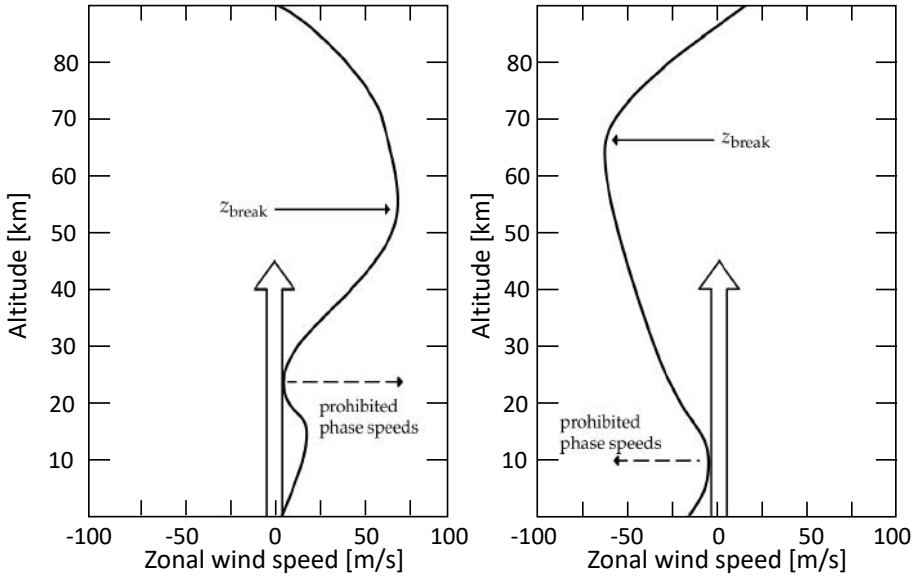

Figure 2.1: Mean wind profiles in January and July and corresponding effects on wave propagation after Lindzen (1981)

Theoretical Description and Modeling

Starting from the Navier-Stokes equations (NSE) several simplifications and approximations matching atmospheric conditions are made, resulting in a set of equations, e.g., models can deal with. A general approach to describe the dynamics of internal waves in a fluid with density stratification and a shear flow in 2D is the Taylor-Goldstein equation (2.3). It is derived from the 2D Euler equations under the Boussinesq assumption and was independently developed three times in 1931, namely by Taylor, Goldstein and Haurwitz. A perturbation velocity u' is introduced to an unperturbed basic flow U.

$$(U-c)^2\left(\frac{d^2\tilde{\phi}}{dz^2}\right)+\left[N^2-(U-c)\frac{d^2U}{dz^2}\right]\tilde{\phi}=0 \tag{2.3}$$

The perturbation is wave-like

$$u' \propto e^{-i\alpha(x-ct)}$$

and the basic flow is $(U(z),0,0)$. The perturbation velocity is introduced through a streamfunction $\tilde{\phi}=\int(u_x dz-u_z dx)$. Hereby c denotes the wave speed and N is the Brunt-Väisälä frequency. Both are complex numbers whose imaginary respectively real part is characteristic for the flow dynamics.
If $Im(c)>0$ the flow is unstable, i.e. a small perturbation is amplified in time. If

$Re(N) = 0$ and $Im(N) \neq 0$ the flow is always unstable (this is called Rayleigh-Taylor instability).
In direct numerical simulation (DNS) of instabilities in mesospheric ice clouds a nondimensionalized version of the nonlinear NSE with Boussinesq approximation is used (Fritts et al. 2017).

Both the scattering of light by particles and also atmospheric dynamics play a major role in understanding the displays of noctilucent clouds. The basics of scattering by particles make clear that using the clouds as a tracer for neutral air motions is limited to timescales where the particle size does not change too much, as the cloud displays become more or less visible with the particle size to the power of 6. On the other hand, atmospheric dynamics on a global scale depend on the transfer of energy and momentum by waves. This transfer induces structures in cloud layers with scales of a few km and time scales in the order of the Brunt-Väisälä period of about 6 minutes (Baumgarten and Fritts 2014).

Chapter 3

Instruments

In order to study small-scale structures in noctilucent clouds, one has to use instruments that are capable of resolving these structures. With modern digital cameras and lidar systems resolutions of under 20 m are possible. In this thesis data from the ALOMAR RMR lidar is used as well as NLC images made by the high-resolution digital cameras of the IAP Camera network in Trondheim, Warnemünde and Kühlungsborn. The stations ALOMAR and Trondheim that will mostly be used are located in Norway, their geographical positions are shown in Fig. 3.1 on the left side.

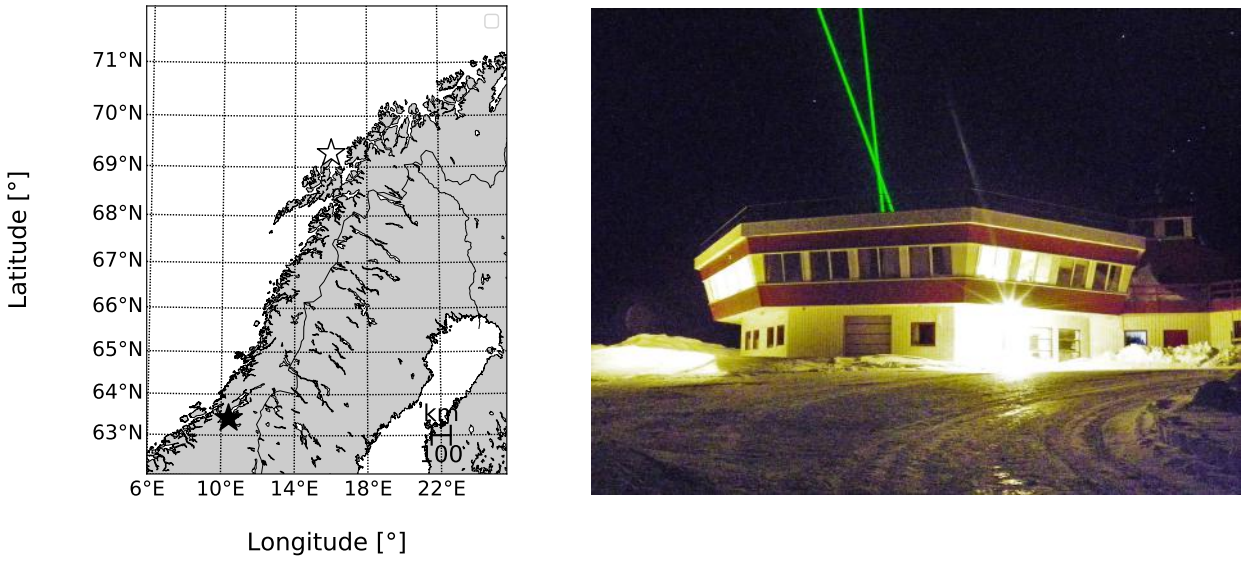

Figure 3.1: Left: Geographic positions of the observation sites (white star: ALOMAR, black star: Trondheim).
Right: ALOMAR observatory with laser.

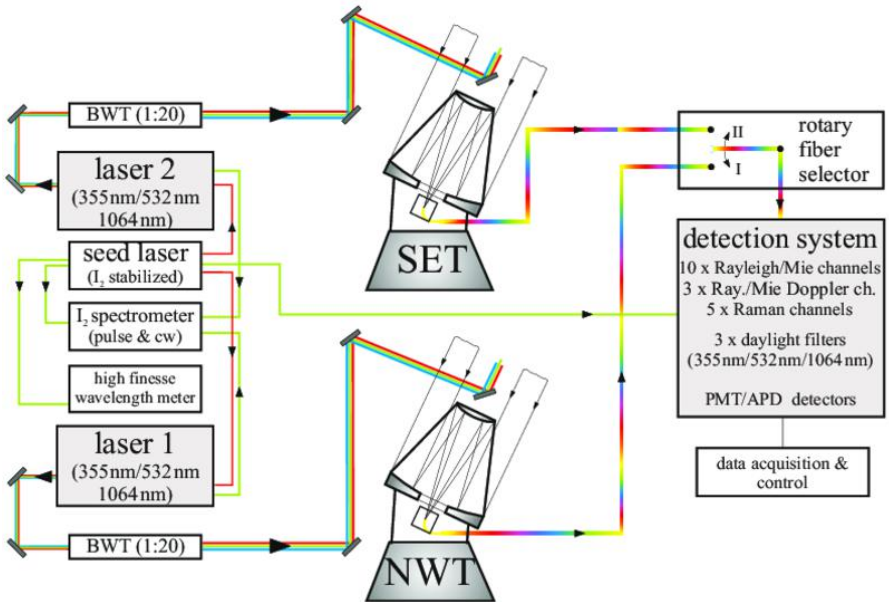

Figure 3.2: Scheme of the ALOMAR RMR lidar: Light is generated by two lasers and received by two telescopes. The backscatterd light is recorded by one detection system. (IAP)

3.1 ALOMAR RMR Lidar

"Lidar" is an acronym for "light detection and ranging". It is a remote sensing instrument where the range to a scattering particle is calculated from the delay time between emitted and backscattered photon. In principle, a lidar consists of three essential elements, namely a transmitter (laser), a telescope and a detector. Since the measurements are not done in a laboratory but in the atmosphere, stray light from the sun cannot be avoided. Therefore it is important to have a very stable laser frequency and etalons with narrow bandwidths in order to filter all stray light before reaching the detector. Considering the aim to measure during the NLC season at high latitudes this becomes even more important. The Arctic Light Observatory for Middle Atmosphere Research (ALOMAR) is located on the island Andøya in northern Norway at 69.3° N, 16.0° E. The duration of the polar summer is about two months there, i.e. the sun never sets between mid-May to mid-July. The abbreviation RMR in ALOMAR RMR lidar stands for Rayleigh-Mie-Raman which represent the three relevant scattering mechanisms.

At ALOMAR an injection-seeded Nd:YAG laser with a wavelength of 1064 nm and its second and third harmonic at 532 nm respectively 355 nm are used. During the seasons contributing to this thesis the power per pulse at 532 nm was 50 MW, the repetition

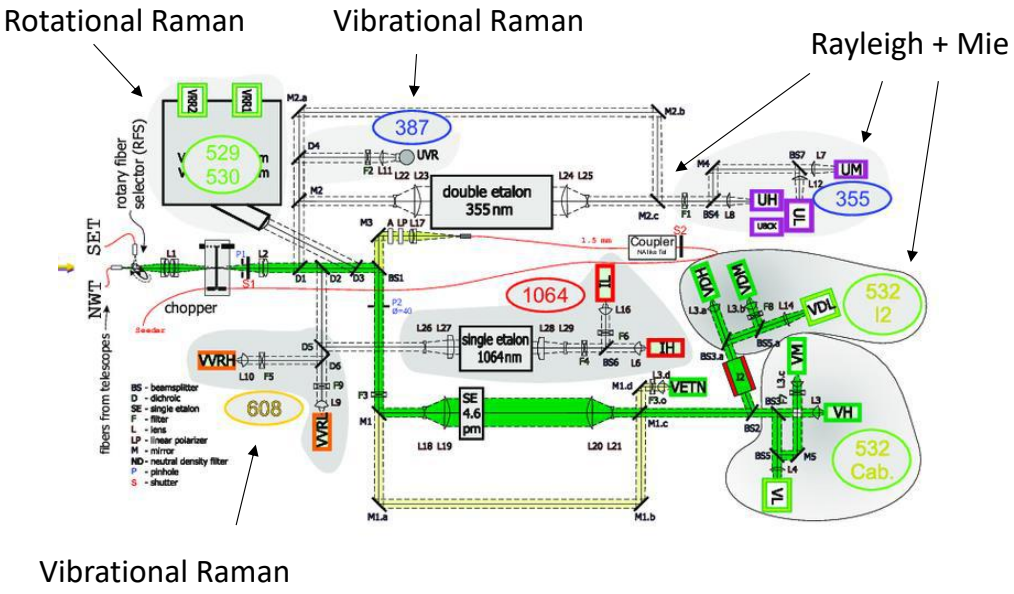

Figure 3.3: Detection unit of the ALOMAR RMR lidar showing the branches for the different wavelengths and scattering mechanisms. (IAP)

frequency was 30 Hz giving an averaged power of ~14 W per laser (Baumgarten 2010). The wavelength stabilization is done by locking the seed laser to one absorption line of a iodine cell. The iodine spectrum has very steep slopes so that a continuous wave seed laser also operating at 1064 and 532 nm can be locked precisely in frequency. Thereby the long-term wavelength drift is limited to less than 0.1 pm. Strong spatial filtering by the 1.8 m diameter steerable telescopes (field of view 100 μrad) and spectral filtering in the detection system (etalon bandwidth of 4.6 pm) makes NLC detection possible even at the highest solar elevations in summer. The alignment of emission and field of view of the telescopes is done using the beam guiding mirrors of the transmitter branch. A CCD camera in the receiving telescope takes a picture of every pulse and compares the position with the desired one. A correction of the outgoing beam is performed by tilting the mirror on top of the telescope structure. The detection unit of the lidar system is shown in Fig. 3.3. A further description of the system is given in von Zahn et al. (2000), updates concerning NLC detection between 1994 and 2017 are listed in Fiedler et al. (2017). In the described setting daytime measurements with the ALOMAR RMR lidar are possible up to 90 km altitude.

NLC data is provided in different temporal resolutions. From the beginning of measurements in 1994 data sets with a temporal resolution of 10 minutes and a range resolution of 150 m are available, since 2008 also a resolution of 30 seconds and 40 m.

Very fast counting electronics and software is required to resolve even smaller structures by counting every laser shot individually. For the ALOMAR RMR lidar such a software is installed since 2011 and is called Lidar Single-Shot Acquisition (LISA). Having a pulse frequency of 30 Hz during the observation years 2011-2018 the temporal resolution of the lidar data is 0.033 s together with a range resolution of 25 m. The range for which LISA data can be recorded spans 50 km.

Measuring the NLC backscatter

A lidar signal is a count rate per time and altitude interval that consists of backscattered light coming from molecules as well as from particles. This is described by the so-called lidar equation

$$\vec{I_i}(\lambda, \lambda_0, r) = A_i \hat{T}(\lambda, r) \frac{\left(\hat{F}_m(\lambda, \lambda_0) + \hat{F}_a(\lambda_0)\right)}{r^2} \hat{T}(\lambda_0, r) \vec{I_0}(\lambda_0)$$

where λ_0, $\vec{I_0}$, λ and $\vec{I}$ are sent respectively received wavelength and intensity, A is the system matrix of the sending branch, $\hat{T}$ are transmission matrices of the atmosphere, r is the distance to the scattering object and $\hat{F}_m$ and $\hat{F}_a$ are backscatter matrices for molecules and aerosols. The r^{-2} dependency accounts for the surface proportions in spherical coordinates. The (Stokes) vector notation accounts for the polarization of light.

Several simplifications can be applied to this equation under certain circumstances and yield a scalar form of the lidar equation: For an ensemble with randomly oriented particles the backscatter matrices $\hat{F}_m$ and $\hat{F}_a$ are diagonal and can be expressed by the volume backscatter coefficient β_v. Under the assumption of single scattering the transmission matrices $\hat{T}$ can be replaced by a factor T times the unit matrix $\hat{1}$ and in the case of linearly polarized light the intensity $\vec{I_0}$ can be written as $\vec{I_0} \propto I_0 \cdot (1, 1, 0, 0)$. As the lidar was recording the backscattered light without analysis of polarization the lidar equation simplifies to:

$$I \propto \frac{1}{r^2} \cdot T^2(r) \cdot I_0 \cdot \beta_v(r) \tag{3.1}$$

Since the detection at ALOMAR is most sensitive to the second harmonic at 532 nm only this wavelength is used for the calculation of β_v. In order to specify the amount of NLC particles present the backscatter ratio $R_\lambda(z)$ of total to molecular backscatter

$\beta_{\lambda,mol}$ is used. The backscatter ratio is

$$R_\lambda(z) = \frac{S_\lambda(z)}{S_{\lambda,mol}} = \frac{\beta_{\lambda,mol}(z) + \beta_{\lambda,NLC}(z)}{\beta_{\lambda,mol}(z)}$$

The product of number density and Rayleigh cross section yields the molecular signal. Hereby the mass density is taken from the MSISE-90 model, the conversion to number density is done assuming a molar mass for air molecules of $m = 28.9652\,\mathrm{g}$ (Picone et al. 2002). The Rayleigh cross section is taken from Bodhaine et al. (1999) using interpolations by Eric Shettle (NRL).

Further the background is removed by taking the average over 10 bins ($\approx 250\,\mathrm{m}$) above the NLC layer and subtracting it from the signal. For the LISA data the background signal $S_\lambda(z)$ is normalized at 45-50 km altitude where no aerosols are expected. 200 height bins ($\approx 5\,\mathrm{km}$) in this region are used for averaging. Then the backscatter

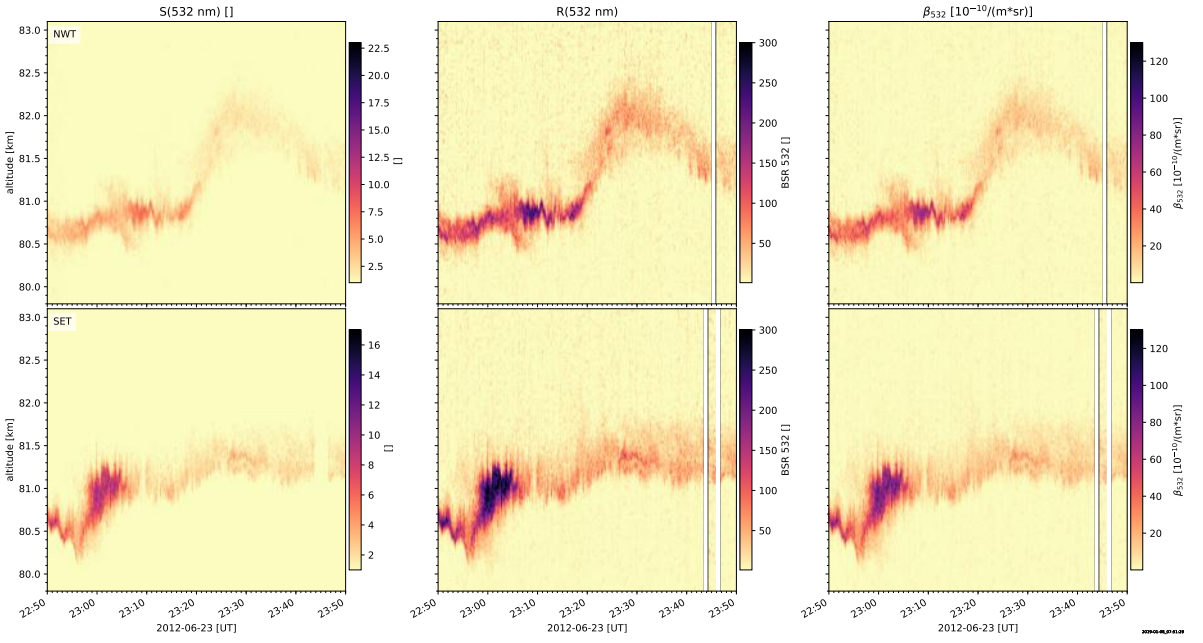

Figure 3.4: Signal (left), backscatter ratio (middle) and NLC backscatter coefficient (right) from LISA data of the ALOMAR RMR lidar on June 23, 2012: The upper row shows data from the North-West Telescope (NWT) pointing 20° off-zenith to the north and the lower row shows data from the South-East Telescope (SET) pointing 20° off zenith to the east. Note the different scaling of the signal panels. The data is integrated for 1 second and smoothed with a Gaussian window with FWHM 11 seconds and 294 m.

coeffifient for NLC particles is calculated as

$$\beta_{\lambda,NLC} = N(z) \cdot \frac{d\sigma}{d\Omega}(\lambda) = (R_\lambda(z) - 1) \cdot \beta_{\lambda,mol}(z)$$

where $N(z)$ is the number density of NLC particles and $\frac{d\sigma}{d\Omega}$ is the backscatter cross section. To simplify the following discussion $\beta_{532} := \beta_{\lambda,NLC}$ is defined. By the transition from signal to volume backscatter coefficient influences from variations in atmospheric transmission and different laser powers are eliminated. In the example in Fig. 3.4 the signal of the North-West telescope is weaker even though the volume backscatter coefficient turns out to be equal. In other cases the differences in the appearance of the three properties are less remarkable. In addition to the volume backscatter coefficient particle sizes derived from the color ratio of the three colors operated by the ALOMAR RMR lidar (1064 nm, 532 nm and 355 nm) are used in this thesis. The particle size information was provided by Gerd Baumgarten and the calculation is described by von Cossart et al. (1999) and Baumgarten et al. (2007).

3.2 NLC Camera Network by IAP

All images used for this thesis are made by the automatic camera network of the Leibniz-Institute of Atmospheric Physics at the University of Rostock (IAP). It contains several high-resolution digital cameras with their field of view directed towards the northern sky. Pictures are taken, stored and transferred to IAP automatically throughout every day of the year. Exposure time, aperture value and ISO speed are adjusted by a control software that takes the solar elevation and the previous image brightness into account. According to that also the time between pictures varies (typically 20 to 60 s). Most relevant for this thesis is the camera in Trondheim ("TROND") (63.4161°N, 10.4074°E) with a field of view heading towards the lidar observation site at ALOMAR. This camera is a Canon EOS 450D with a lens of 28 mm focal length. Other cameras are located in Kühlungsborn at IAP ("KBORN") and on the roof of the Leibniz-Institute for Baltic Sea Research, Warnemünde ("IOW"). Both are Canon EOS 550D models.

Chapter 4

Data Analysis

Motivation

The lidar single-shot acquisition software LISA is installed at ALOMAR since 2011. So the dataset spans the summer seasons from 2011 to 2018. An average NLC season at ALOMAR lasts from June 1 to August 15, even though earlier detections from mid-May and later NLC until the end of August occur in several years (Fiedler et al. 2017). During this period the total measurement time is 150-460 hours per year where NLC are detected during 100-300 hours. So the database to study small-scale structures is huge (about 1600 hours) and for different applications certain events are selected and discussed in this thesis.

An example for how the single-shot acquisition reveals structures that have not been visible before is given in Fig. 4.1. The upper border of the layer is visible in a much more detailed way in the upper picture, e.g., the spikes at 02:51 UT are not visible in the 30 s data at all. In general, it becomes clear that height variations which appear as jumps in the 30 s data always become continuous motions in a higher resolution. Another feature that occurs frequently are parallel moving layers with a very small vertical separation below 200 m. From 03:00 to 03:05 the lowest of the three layers can only be adumbrated in the lower, while its parallel movement is clearly visible in the upper plot.

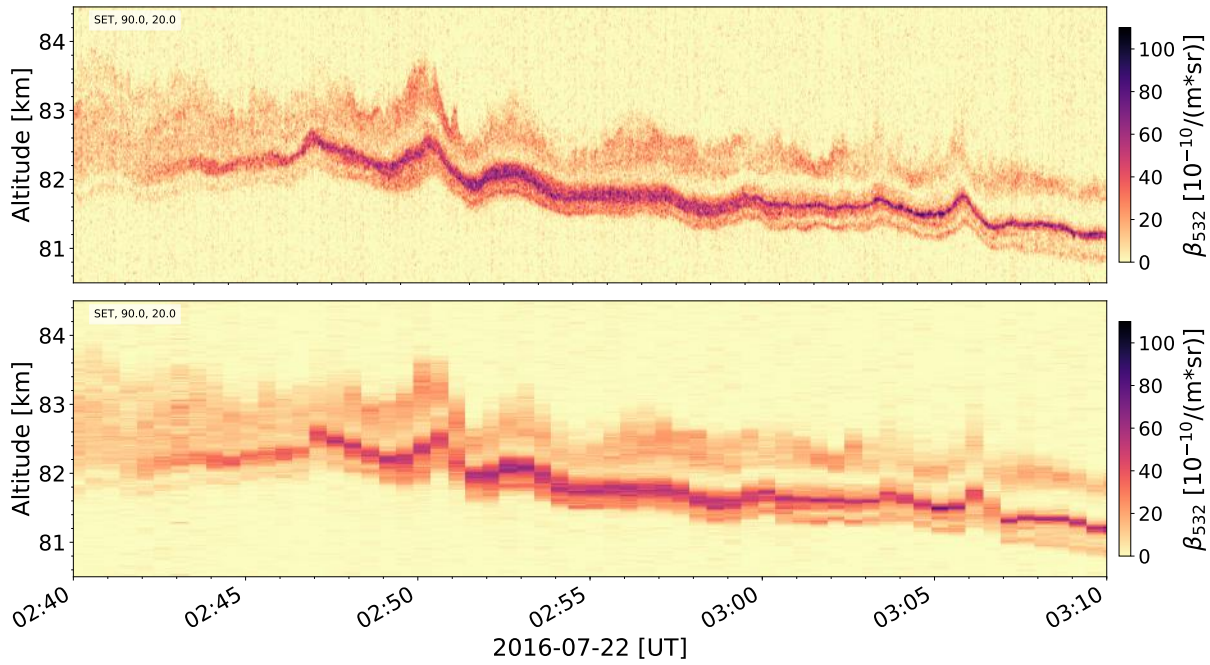

Figure 4.1: NLC backscatter coefficient in ALOMAR lidar data from July 22, 2016, 02:40 - 03:10 [UT]: The upper panel has a resolution of 1 s from the single-shot acquisition software, the lower picture shows the same data integrated for 30 s. The name and orientation of the telescope are given in the upper left corner, where the first number is the azimuth and the second number is the angle from zenith. The color scale represents the NLC backscatter coefficient at 532 nm β_{532} in $10^{-10}/(\mathrm{m} \cdot \mathrm{sr})$.

4.1 Lidar Data

4.1.1 Data Selection and Preprocessing

Lidar data with 30 s temporal resolution is plotted on a routine basis during every measurement. By looking at these plots from all NLC events during the years 2011 until 2018, cases with rapid changes in NLC structure and height were identified. It is expected that strong vertical displacements of NLC layers are connected to instabilities or even overturning waves.

Since the single-shot data is too large to be plotted in full resolution, it is integrated in time again to a resolution of 1 s. For the selected cases, the NLC backscatter coefficient is then plotted in one-hour intervals. During events where the NLC is more or less single-layered, the centroid altitude is calculated in order to determine a temporal spectrum of vertical movements (see 4.1.3).

4.1.2 Categorization of Small-scale Features in High-resolution Lidar Data

The aim of using the single-shot acquisition software LISA is to resolve wave signatures, instabilities and mixing processes in NLC on the smallest scales possible with the ALOMAR RMR lidar in the current setup. Already in 2017 studies were performed where 2D-pattern recognition was applied to identify wave structures in NLC data with 30s resolution (Ridder et al. 2017). Compared to the resolution of 10 minutes typically used in other lidar instruments, new features were found and described. Looking into the LISA data with even higher resolution so many different and individual patterns are discovered that it currently is not meaningful to apply a similar pattern recognition technique as before on even smaller scales. Instead, a characterization of the events is made individually and new categories are defined and assigned to them.
In the style of the types for NLC structures in images defined by Fogle and Haurwitz (1966), the following categories to identify patterns in NLC focusing on vertical structure and the occurrence of instabilities are proposed:

I. Thin layers (< 500 m)
   a) Smooth drift, wave periods > 10 min, associated with unperturbed waves.
   b) Short period height variations (< 5 min), either short period waves or irregular height variations.

II. Layers of middle thickness (0,5 - 1 km)
   a) Smooth drift, wave periods > 10 min, associated with unperturbed waves.
   b) Short period height variations (< 5 min), either short period waves or irregular height variations:
      i. Constant vertical density profile throughout the layer.
      ii. Higher density at the upper or lower limit of the layer.

III. Thick layers (> 1 km)
   a) Density distribution temporally even, without short period height variations:
      i. Constant vertical density profile throughout the layer.
      ii. Higher density at the upper or lower limit of the layer.

b) Irregular structure in time and range (thickness of the layer may vary with changing substructure).

c) Multi-layer composition:

   i. Parallel movement of the layers.

   ii. Non-parallel movement of layers, including creation and extinction when entering/ leaving a certain height region.

Examples for all types are given in Fig. 4.2-4.4. The definition of the types is mainly based on empiricism, reflecting the observed structures. The differentiation starts with separating NLC layers by thickness since this indicates the range in which the background conditions are suitable for NLC during that particular event. Category III is divided into more subtypes than category I since a thicker layer can involve a lot more phenomena inside.

Small-scale structures are especially addressed by the categories I b, II b, III b and III c. The differentiation between a constant vertical density profile throughout the layer and a higher density at the lower or upper limit of the layer in the categories II b and III a is made on different purposes: On one hand particle sizes are the most important factor for the visibility of NLC and they typically vary throughout the layer. Larger, heavier particles are more often located at the lower boundary of the NLC layer, so in type II b ii and III a ii a higher percentage is expected to have a maximum backscatter at the lower boundary. On the other hand, the behavior of these lower (or upper) boundaries can be compared with the movements of thin single layers or layers inside a multi-layer type (III c). Type III b is a pool to collect cases that cannot be assigned to another category due to the presence of many structure types at the same time. Since there are many different variants of type III b several examples are shown.

4.1.3 Spectral Analysis

A spectral analysis of small-scale structures in lidar time series is performed in order to provide evidence for the presence of oscillations in NLC altitudes down to very small scales and to investigate whether the spectra can be used for detection of enhanced and interesting variations in NLC. For that purpose different profiles are calculated and analyzed. On temporal scales altitude variations of the centroid altitude z_c are used. For type I NLC one can use the centroid altitude as robust tracer for vertical motion.

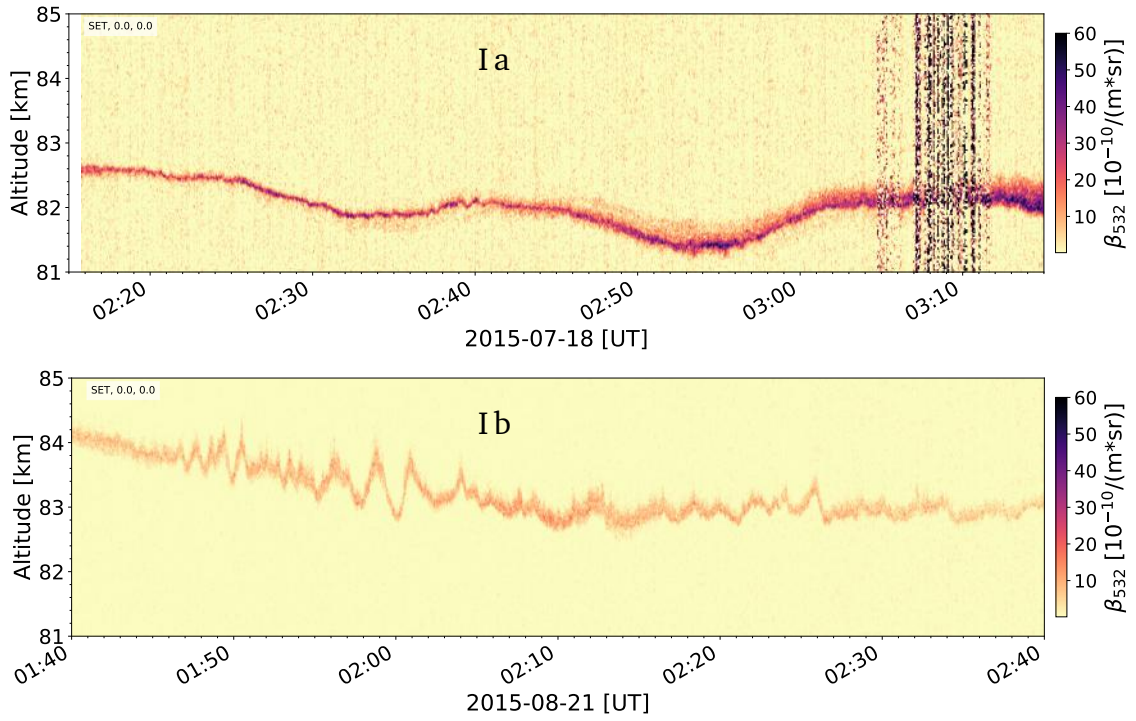

Figure 4.2: NLC layer profiles for two measurements on July 18, 2015, (upper panel) and August 21, 2015, (lower panel): The boxes in the upper left corner indicate the name of the telescope and its orientation. Times with low signal to noise ratio appear as vertical lines with a dark shaded pattern.
Upper panel: type Ia, lower: type I b

The centroid altitude is defined as:

$$z_c = \frac{\Sigma \beta_{532}(z_i) \cdot z_i}{\Sigma \beta_{532}(z_i)} \tag{4.1}$$

Here $\beta_{532}(z_i)$ is the NLC backscatter coefficient in an interval at altitude z_i.
For the calculation of power spectra a method similar to Kaifler (2013) is used that applies a Morlet wavelet transform of order 6. They used the LISA raw data of selected events with high-quality data (very little variations in atmospheric transmission). Now for the first time background reduced and normalized signals are processed, namely the volume backscatter coefficient β_{532}. In order to achieve comparable results, the selection of 10-minute intervals is kept since an interval of 10 minutes is suitable to resolve frequencies lower than the Brunt-Väisälä frequency N that is about 5 min under these conditions. For the calculation of the centroid altitude a height range of 2 km around the NLC altitude is used.

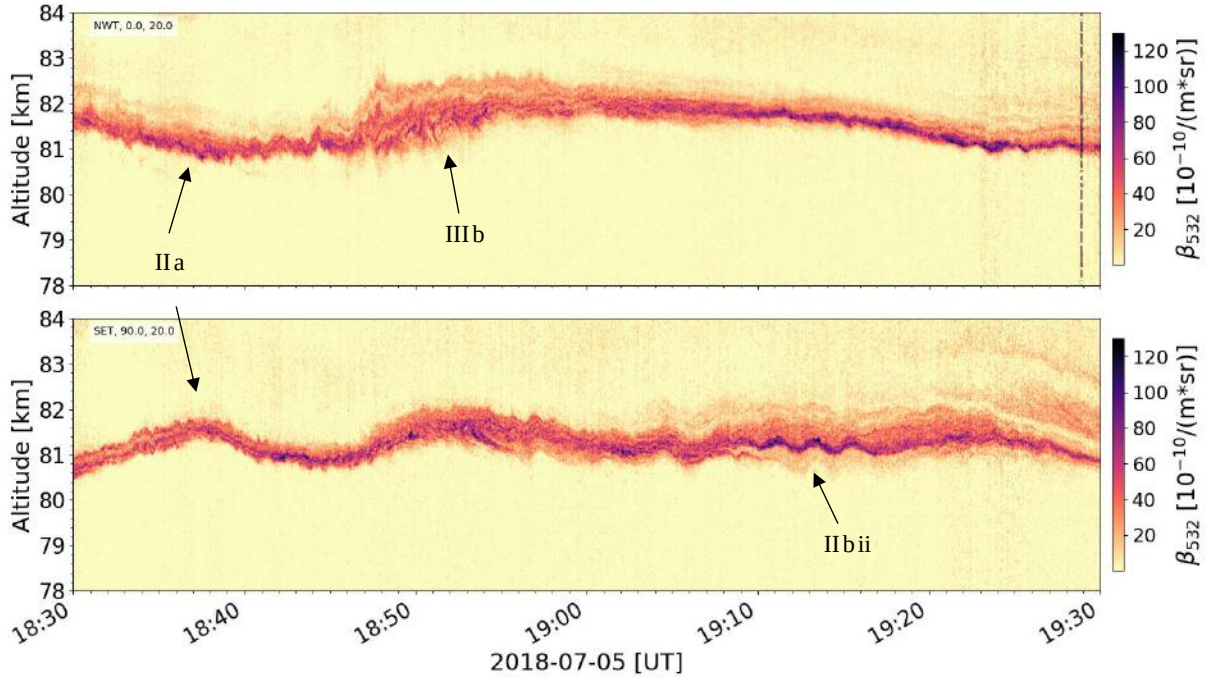

Figure 4.3: Types II a, II b ii and III b as labeled. Here the two telescopes were pointing 20° off-zenith towards North (upper panel) and East (lower panel).

Interpretation of Profiles from Tilted Telescopes

Due to the tilting of the telescopes, the data is not acquired in vertical direction originally, but the altitude of the signal is stored using a correction factor for the prolonged range. Nevertheless, in a layer of a few kilometer thickness one point in the upper border is not located above a point of the same record at the lower border of the layer. The horizontal separation is demonstrated in a sketch in Fig. 4.5. Taking a horizontal wind value of 40 m/s which is typical at NLC altitudes according to Fiedler et al. (2011), the time a structure needs to travel the distance s is estimated. The resulting advection time is between 5 and 30 s. This time is relatively short compared to the plot intervals of 1 hour in Fig. 4.2-4.4 indicating that the angle one has to keep in mind when interpreting the plots is small. In contrast, 30 s is generally a long time when analyzing data with a resolution of 33 ms. When for example interpreting vertical spectra, thick layers are of interest and for those the data should be aligned in time according to the background wind.

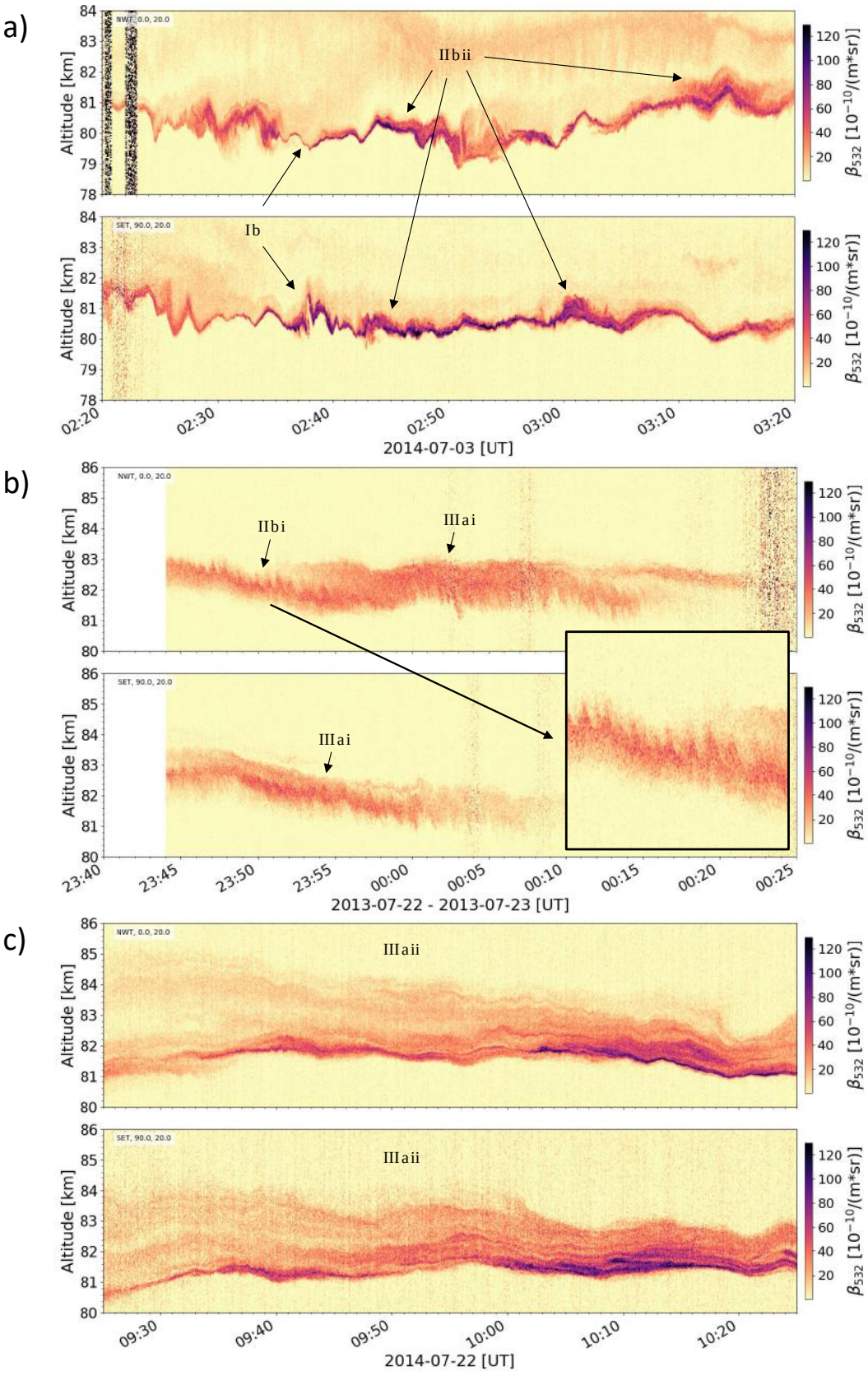

Figure 4.4: a) Type I b and II b ii as labeled, b) type II b i and III a i as labeled, c) type III a ii.

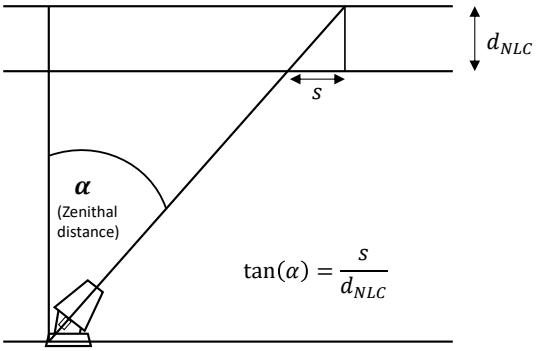

For the standard zenithal distance angle α of the ALOMAR telescopes in wind position, which is 20°, $\tan(\alpha)$ is 0.364. That means the horizontal separation s of two points is 364 m per kilometer vertical separation d_{NLC}.

Figure 4.5: Vertical vs. tilted range of a lidar beam.

4.2 Camera Images

4.2.1 Brightness Spectra

Mapping of Images

In order to resolve small-scale features in NLC without distortion due to viewing geometry the images are unwarped, i.e. projected onto a plane horizontal surface. Star traces in the images are used to determine the exact field of view of the camera (FOV) as well as the orientation parameters azimuth, elevation and rotation. This method is shortly summarized here, a detailed description is given in Schäfer (2016). In principle one only needs to see two stars per image and to know their viewing angles for the given geographic position of the camera. The latter is determined by GPS to an accuracy of order 10 cm. Additionally the field of view of the camera must be known in this case, e.g. calculated from the sensor length d and the focal length f with $\delta = 2 \cdot \arctan(\frac{d}{2f})$. More accurate results are obtained by using more stars and longer time periods. Using the image library PIL it is possible to overlay consecutive pictures and fit the star traces to the expected traces provided by a database. By comparison of the trace ends' positions even a possible time shift caused by an inaccurate computer clock can be eliminated. As the projection of the lens the Slant Zenithal Perspective (SZP) is applied for the digital camera in Trondheim, the Gnomonic Tangent Plane (TAN) for the Warnemünde camera and the Zenithal Perspective (AZP) for the camera in Kühlungsborn. The field of view is interactively adjusted to the star traces as well as the orientation parameters. The results for the relevant nights and stations are given in table 4.2.1. An example

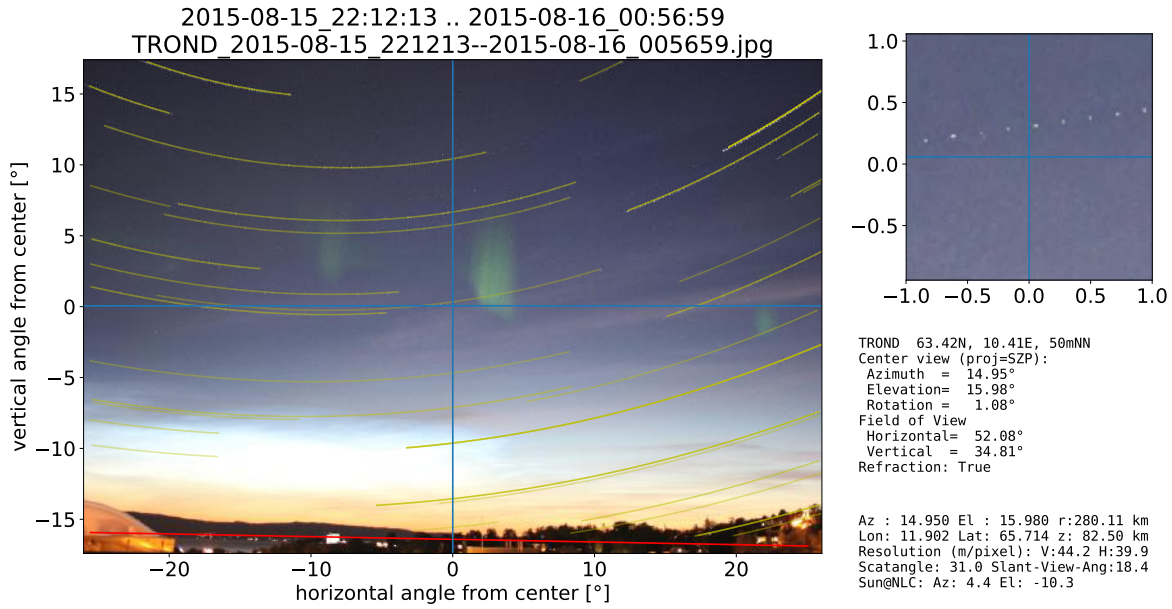

Figure 4.6: Orientation and field of view of the TROND camera on August 15, 2015: White dots are stars in the images, yellow lines are calculated star traces and the red line indicates the horizon. The values in the lower right corner correspond to the blue cross. The lower part of the sky is bright due to NLC, the green spots are arising from aurora borealis.

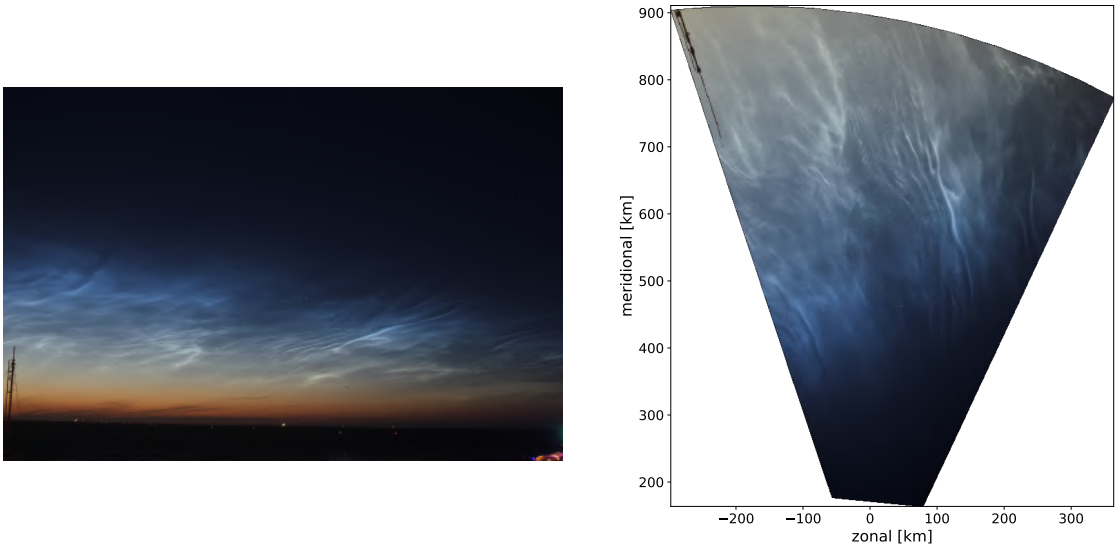

Figure 4.7: Original (left) and projected (right) NLC image from Warnemünde, Germany, taken on July 10, 2015: The meridional and zonal axis in the projected image denote the distance to the camera site.

for a finally adjusted set of star traces is given in Fig. 4.6, an example for original and mapped image is shown in Fig. 4.7.

station	date	az. [°]	elev. [°]	HFOV [°]	VFOV [°]	rot. [°]
TROND	July 23-24, 2014	15.53	17.42	51.40	34.49	-0.09
	August 15-16, 2015	14.95	15.98	52.08	34.81	1.08
	August 16-17, 2015	14.95	15.98	52.08	34.81	1.08
KBORN	July 11-12, 2016	13.75	9.48	47.60	31.59	-0.29
IOW	July 10-11, 2015	3.10	12.47	47.60	31.59	1.30

From the mapped images it is possible to extract the brightness as series along intersections through the picture. As a direction for these profiles zonal and meridional lines are chosen. For each intersection a wavelength spectrum is calculated and averaged for all profiles of the same direction using Welch's method (Welch 1967). In total about 15 images with NLC were analyzed and selected results are presented in chapter 5.2.

4.2.2 Extraction of Brightness Time Series from Camera Images

Combining camera and lidar measurements is a powerful tool to get a wider view of the dynamics observed in NLC since the lidar delivers altitude resolved information at one or two locations while the camera delivers horizontal information of the vertically integrated layer. To investigate similarities and differences between the two methods time series from camera images are extracted to be compared with vertical and temporal scales from lidar observations. In the last years IAP has intensified the efforts to capture simultaneous lidar and camera observations. In 2014 and 2015 a few events were recorded where the ALOMAR RMR lidar detected NLC at the same time as the camera in Trondheim photographed them. This section presents these simultaneous lidar and camera observations of the same NLC and compares the brightness series directly.

Since the brightness values are subject to many underlying variables one after another have to be specified. First, the calculation of the brightness will be introduced. The color of a pixel is stored in the RGB format. In principle, different approaches to obtain the pixel's brightness are thinkable:

I. In the definition of luminance that is, e.g., used in television signals and implemented in many image converters, all three channels are used and in different weights (ITU 2015). The weighting which is 0.2126R$+0.7152$G$+0.0722$B refers to the sensitivity of the human eye to these colors.

II. It is possible to select a certain color or a combination of colors that is best suitable for the application on noctilucent clouds. Earlier studies by Schmidt (2013) addressing the automatic detection of NLC in camera images report that the contrast between background and NLC is strongest in the blue channel.

Here the choice of the blue channel is made. Then the brightness of the image at certain points is extracted, namely for the NLC volumes where the lidar performs measurements. To find the pixels associated with these volumes the geographical coordinates of all image points are calculated on the ellipsoid of the World Geodetic System WGS 1984 as provided by the python package proj4 and stored as matrices. More details on this mapping technique are found in Kondabathula (2018). By mapping the images to a horizontal plane latitude and longitude coordinates are allocated to all image pixels under the assumption of an a priori defined NLC altitude. When finding the beam positions' geographical coordinates in the stored matrix the smallest root mean square deviation is used. The error is in the order of 0.003° in longitude and latitude.

Since the NLC altitude is changing in time a technique needs to be introduced to approximate how many pixels have to be taken into account in order to cover a typical height range. For the latter a range from 81.5 km to 84.0 km seems reasonable for visible NLC events. Therefore the lidar beam positions, as well as the matrix containing all pixels' latitude and longitude, are computed for the assumed NLC heights 82.0 km, 83.0 km. The results are given in table 4.1. From the difference in the pixel indices it follows that 9 pixels in the vertical direction correspond to 1 km displacement in altitude (pixel numbers x=2962-2970 for zenith in 2015). So the altitude range 81.5 km to 84 km is represented by 21 pixels (x=2954-2974 for zenith in 2015). Since the difference in the orientation of the cameras in 2014 and 2015 is small, the same number of pixels per kilometer is taken into account in both years.

For a correct interpretation and comparison of the camera time series with lidar data several technical and physical aspects have to be taken into account. On the technical side exposure time, aperture value and ISO speed of the camera influence

	altitude [km]	az [°]	zda [°]	range [km]	lat [°]	lon [°]	x pixel	y pixel
2014								
NWT	83	0	20	87.8	69.5444	16.0086	3033	2800
SET	83	90	20	87.8	69.2769	16.7595	3012	3125
2015								
Zenith	82	0	0	81.6	69.2785	16.0086	2970	2925
Zenith	83	0	0	82.6	69.2785	16.0086	2962	2925

Table 4.1: Geographical coordinates of NLC positions of the ALOMAR RMR lidar beams depending on telescope pointing (az: azimuth, zda: zenith distance angle) and NLC range together with their corresponding pixels in the original images (not mapped): The x direction is vertically oriented in the image, y is the horizontal direction (e.g. left panel in fig. 4.7).

the brightness of image pixels. Serendipitously exposure time and aperture value turn out to stay constant during the relevant periods. Nevertheless, the ISO speed varies for some of the events. Its quantitative impact on the absolute brightness is not known, i.e. the adjustment has to be made such that the change from one picture to the next is set zero when an ISO jump occurs. The used brightness unit scales linear in RGB pixel values and is normalized to the value at the starting time which is set zero. Due to that only variations are considered afterward and no quantitative comparison with volume backscatter coefficients from lidar observations is possible. It remains also questionable if the amplitude of brightness changes has to be scaled due to the variation in sensitivity. Nevertheless, this impact cannot be quantified and has to be neglected. Anyway, the aim to observe trends and correlations between lidar and camera observations can also be obtained with relative rather than absolute values.

Physical aspects influencing the brightness are primarily given by the sun position that affects the scattering angle and the elevation of the NLC that affects the transmission through the atmosphere. For camera observations the geometry is shown in Fig. 4.8. These aspects will be discussed together with the results in chapter 5.3.

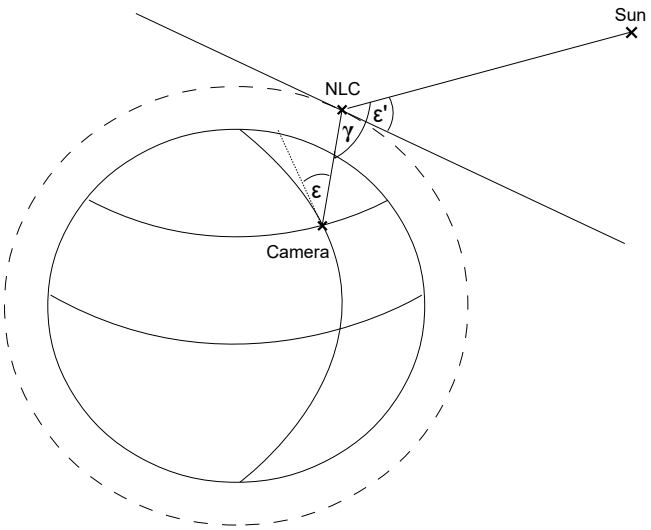

Figure 4.8: Scattering geometry for sunlight, NLC and camera: ϵ' is the elevation angle of the sun seen from the NLC, ϵ is the elevation angle of the NLC seen by the camera. γ is the scattering angle.

Chapter 5

Results & Discussion

5.1 Lidar Observations

Statistics of Small-scale Features

For a statistical analysis of the occurrence of the structure types defined in 4.1.2 the amount of data has to be reduced to one season. The NLC season 2014 is selected due to the longest duration of NLC detection in total. Due to the focus on events with rapid altitude changes and the selection of bright NLC, a subset of the total set of 270 hours as reported by Fiedler et al. (2017), table 1, is taken into account. 189 hours used here which is sufficient to get an overview of the presence of certain features.
For the categorization plots in one-hour intervals are used. The types assigned to the plots are stored in a table together with the time of the record. If two different types occur, they are both stored and each of them is assigned half an hour in the final evaluation. The accuracy of the calculated occurrence time of each type is limited by the plot intervals of one hour. The times are not weighted with the presence of these structures or the duration of NLC detection inside this frame. The begin of each plot interval is chosen such that it starts with the first NLC detection, but sometimes the layer vanishes before the plot interval ends. Then, nevertheless, the type is taken into account as one full hour.

The histogram of the occurrence of the NLC types defined in 4.1.2 is given in Fig. 5.1. Thick layers (type III) of $> 1\,\mathrm{km}$ thickness occur more than half of the time (55%), followed by middle thick layers (type II) at 28% and thin layers ($< 500\,\mathrm{m}$, type I) at 17% of the time. To demonstrate how rich the structures in type III NLC

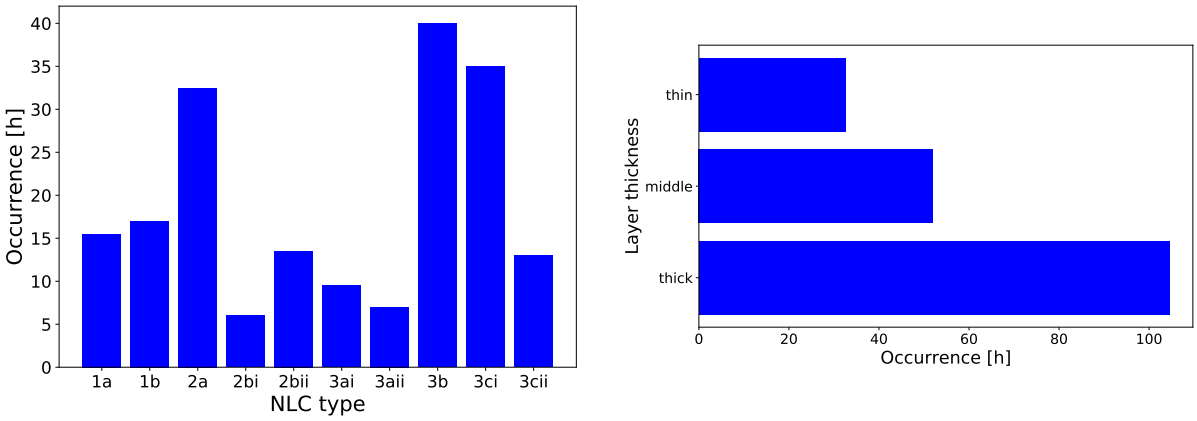

Figure 5.1: Right side: Number of occurrence of the different NLC types defined in 4.1.2 during the NLC season in 2014.
Left side: Integrated numbers for thin (< 500 m, type I), middle (0.5 - 1 km, type II) and thick layers (> 1 km, type III). A total amount of 189 hours has been analyzed.

are some other examples for type III b and III c are given in Fig. 5.2 and 5.3. In a bit more than half of the cases with a thin layer altitude variations on time scales under 5-10 min are detected. In contrast, for middle thick layers category II a dominates, i.e. smooth drifts with longer wave periods. In category I b the example shown in Fig. 4.2, lower panel, is an event showing extremely sharp edges in the oscillations. In other cases the oscillations look sine-like, e.g. in the lower panel of Fig. 4.3 from 19:10 to 19:20 UT. Often the oscillations occur with durations less than one hour or at least changing their shape remarkably during one hour: In Fig. 4.4a, second panel, first oscillations with sharp edges are observed. Afterward they become smoother for a few minutes before irregular variations take over. All three stadiums are passed in only 15 minutes. However, a real jump of the layer as on July 3, 2014, at 02:40 UT is very rarely observed.

Another rare case is the type II b i showing small-scale oscillations in layer of 0.5 - 1 km thickness and a constant vertical backscatter profile inside the layer. It is only detected during 6 h in the while season. Among the cases in category II b the version with a higher backscatter coefficient at the lower or upper border occurs more than double as often (13.5 h). Out of this time there are 2 h where the maximum is at the upper boundary, otherwise the lower boundary is stronger. In thick layers the type with irregular temporal and vertical structure occurs most often, the type with parallel moving layers comes next. In category III c i the separation of layers varies on a range from under 200 m to more than 2 km. The number of parallel layers ranges from 2 to 5.

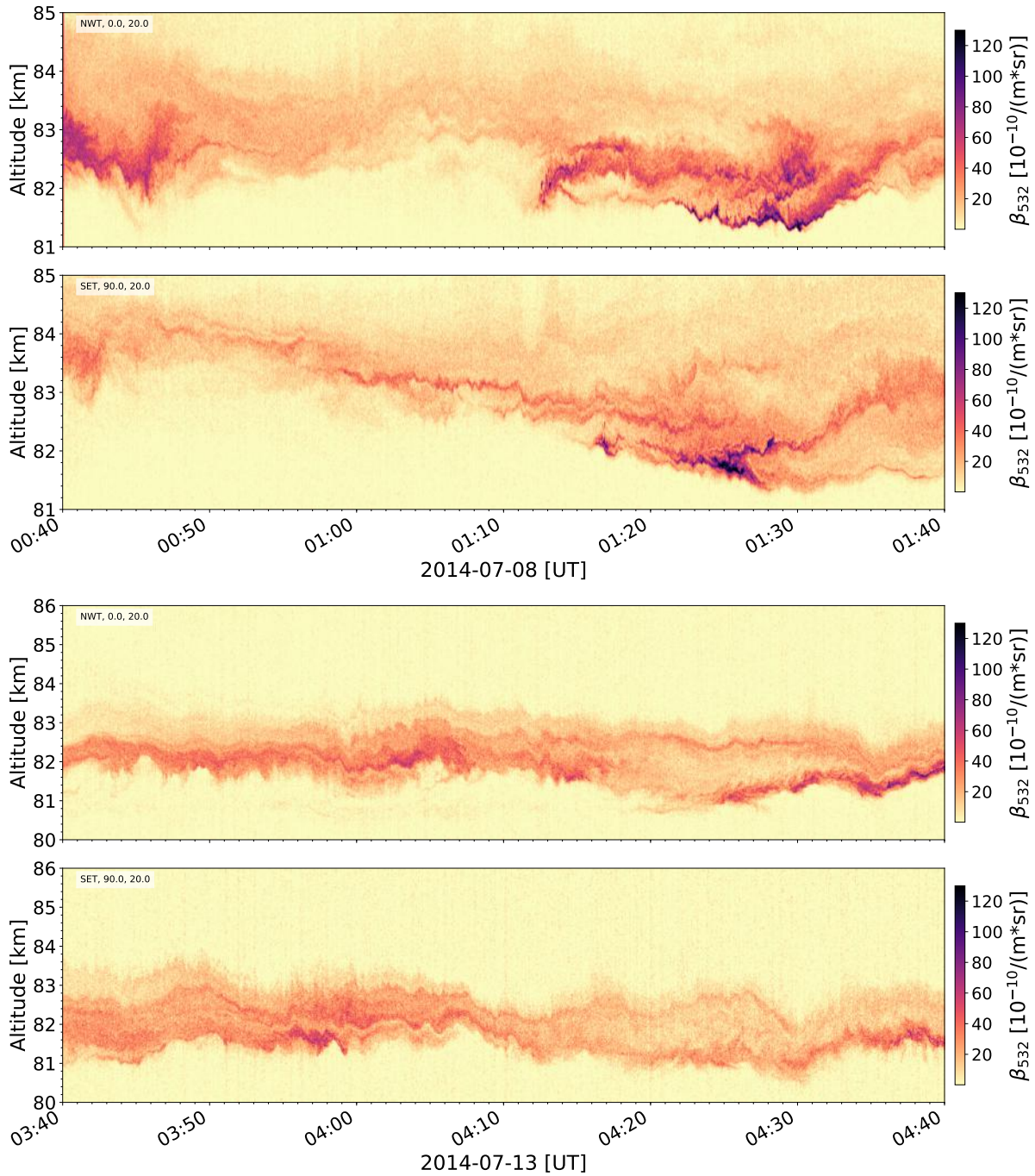

Figure 5.2: Examples for NLC type III b on July 8, 2014, and July 13, 2014: For both measurements the telescopes were tilted 20° to north and east, giving a horizontal separation of about 40 km at the height of the NLC.

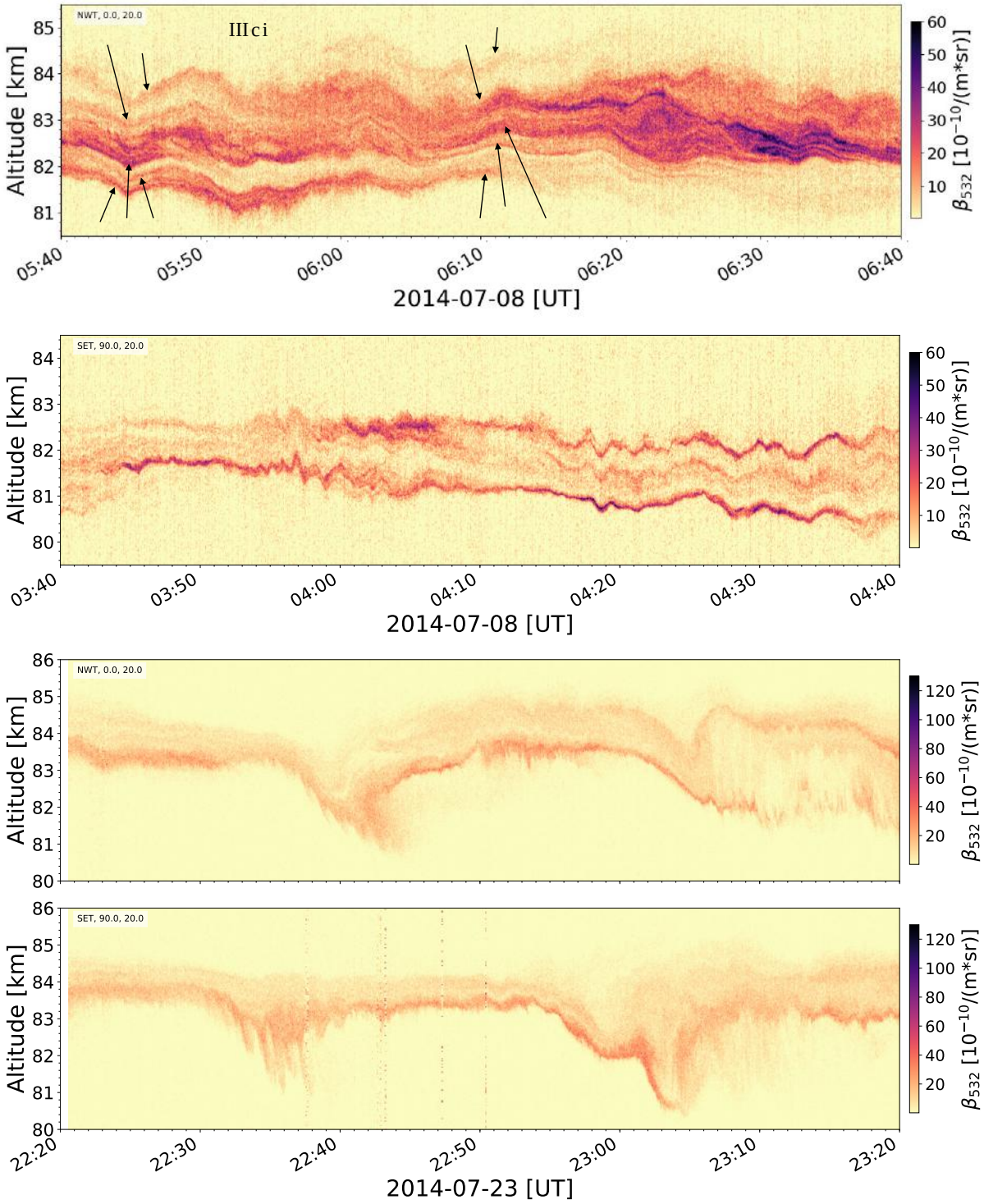

Figure 5.3: Examples for type III c i (upper two panels) and III c ii (lower panel): The first example for type III c i shows the maximum number of 5 layers indicated by arrows, the second example shows a case with a larger separation between parallel moving layers.

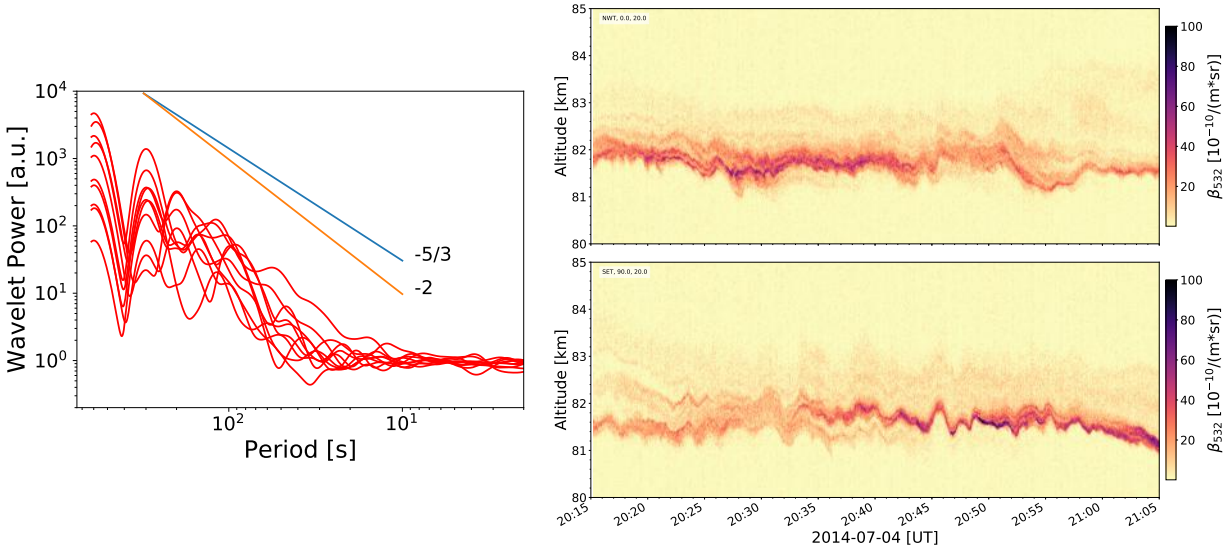

Figure 5.4: Left side: Wavelet power spectrum of NLC centroid altitude on July 4, 2014, for 10-minute intervals between 20:15 and 21:05 UT: The slope of the spectrum is -2.0, the slope of -5/3 from the gravity wave spectrum by Nastrom and Gage (1985) is drawn for comparison.
Right side: NLC backscatter coefficient during the time centroid altitudes are calculated.

Spectral Analysis

One NLC event showing a majority of type I is selected for the spectral analysis (July 4, 2014, 20:15 - 21:05 UT). The power spectra of centroid altitudes were calculated for time intervals of 10 minutes. The result is shown in Fig. 5.4, left side, and shows a slope of -2.0. This is in accordance with the result of Kaifler (2013). On very short timescales below 10 s the spectrum becomes flat due to solar background and photon counting noise. For gravity waves on horizontal scales smaller than 600 km a slope of -2/3 is typical (Nastrom and Gage 1985). Assuming a mean horizontal wind speed at NLC altitudes of 40 m/s reported by Fiedler et al. (2011) the time scales in Fig. 5.4 correspond to horizontal scales of 400 m to 24 km. So at the very short wavelength range scales even below those published by Nastrom and Gage (1985) (smallest scale ~4 km) are resolved. In the spectral range observed by the lidar, the Nastrom-Gage spectrum gives different slopes for winds and potential temperature. However, it is remarkable that NLC repeatedly show a spectral slope of -2 for scales of seconds to minutes corresponding to a few hundred meters to a few ten kilometers.

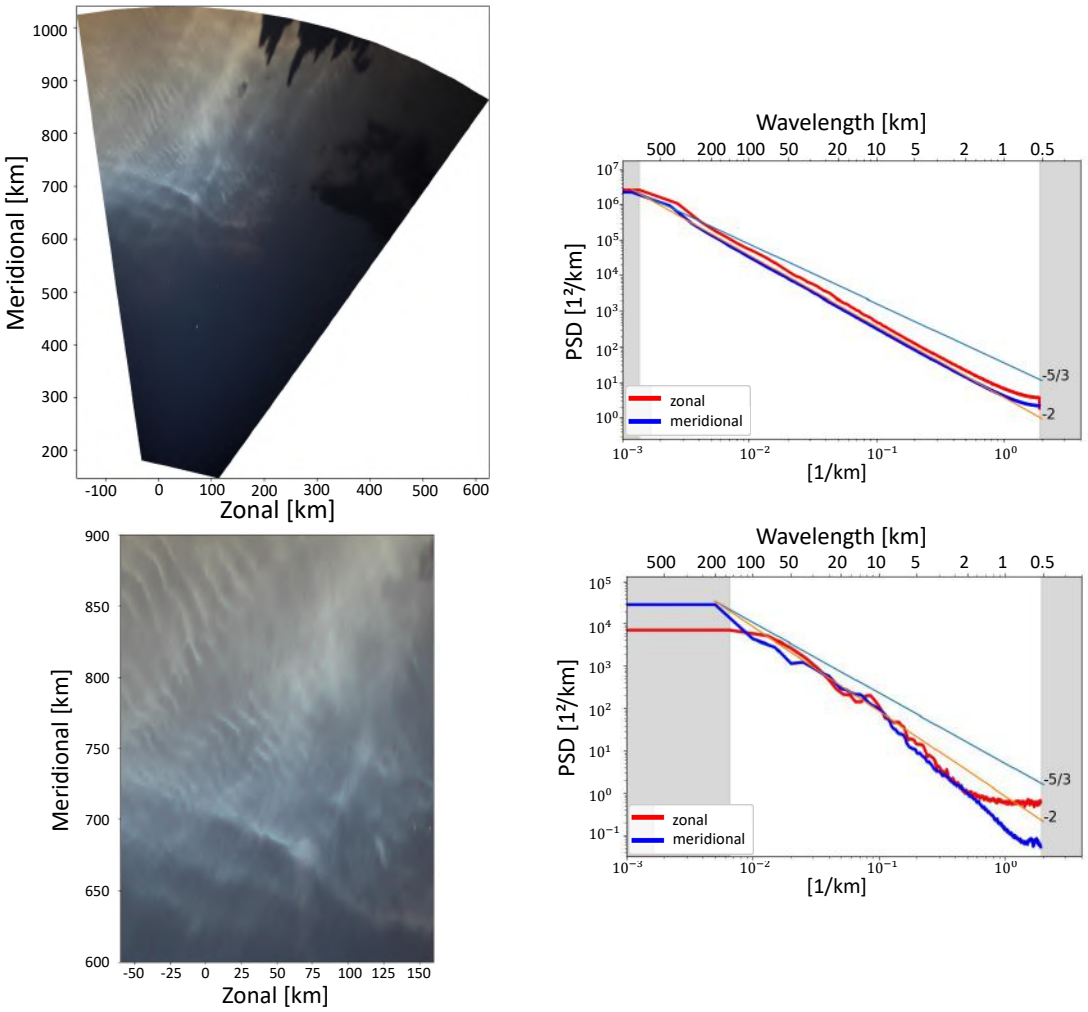

Figure 5.5: Left: Mapped view of an NLC event observed 22:06:15 UT on July 11, 2016, from Kühlungsborn.
Right: Average horizontal wavelength spectrum.
The gray areas indicate the average scales where the spectrum is affected by sampling frequency or length of the dataset.

5.2 Camera Observations

Spectral Analysis

In the following horizontal wavelength spectra calculated directly from two selected noctilucent cloud events are presented: in Fig. 5.5 for July 11, 2016, in Kühlungsborn and in Fig. 5.6 for July 10, 2015, in Warnemünde, Germany. For each case about 1600 spectra in zonal and meridional direction were calculated and then averaged, resulting in the the smooth spectra shown in the figures. Although monochromatic waves are

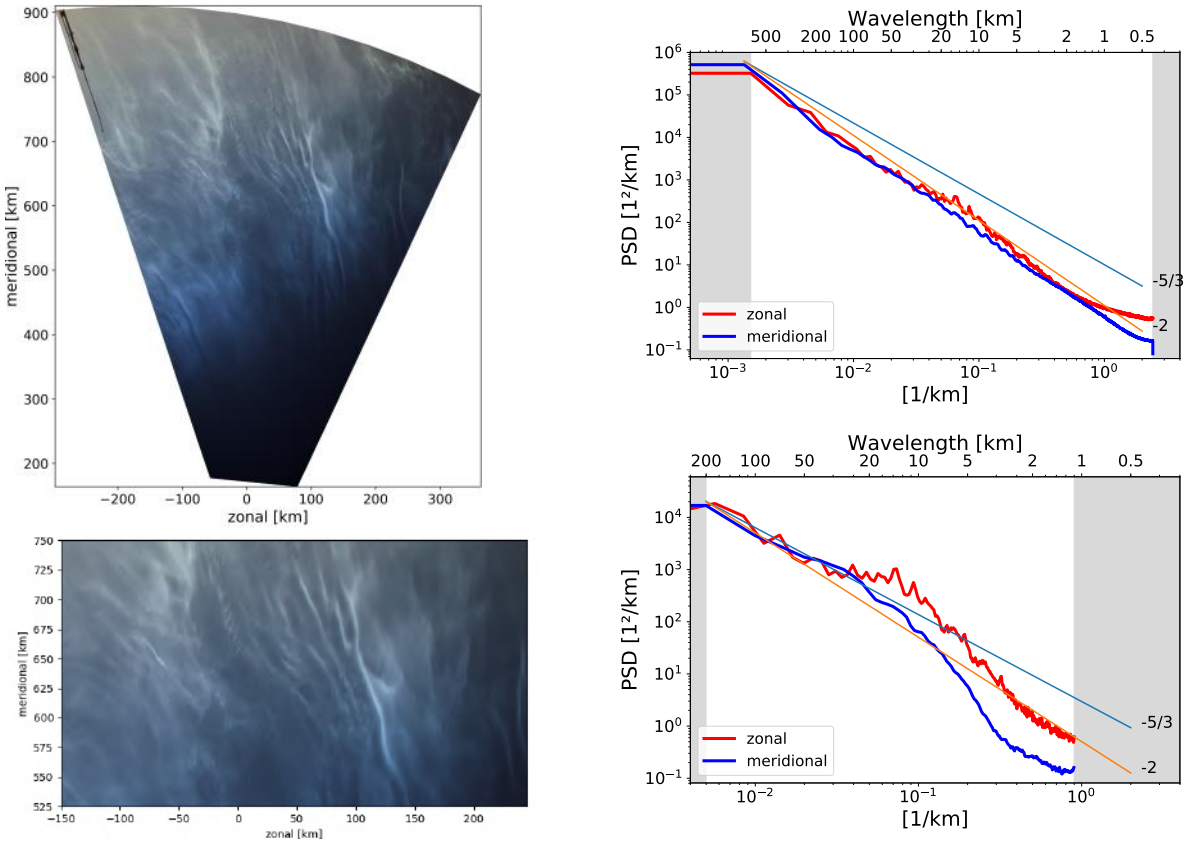

Figure 5.6: Left: Mapped view of an NLC event observed 21:42:49 UT on July 10, 2015, from Warnemünde.
Right: Average horizontal wavelength spectrum.
The gray areas indicate the average scales where the spectrum is affected by sampling frequency or length of the dataset.

visible in the picture the spectrum reveals that wave motions are present on all scales. The slope of the global spectrum is -2.0 in both cases. Peaks for certain wavelengths get higher when regions of the whole image are analyzed. On July 10, 2015, these are the wavelengths 12 km and 16 km in the zonal regime, on July 11, 2016, it is a peak from 13 km to 14 km, also in the zonal spectrum. Smaller peaks are at 5.5 km and 3.8 km for July 10, 2015, and 3.6 km on July 11, 2016, before the spectrum becomes flat. It is striking that in all cases except for the global spectrum from July 11, 2016, the zonal spectrum shows more variations than the meridional spectrum which appears very smooth. This is independent of the format of the analyzed region. On July 10, 2015, the cutout is longer in zonal direction while on July 11, 2016, it is longer in meridional direction. In the global spectrum on July 11, 2016, both spectra are smooth.
The slope of the spectrum from camera images agrees with the spectrum from lidar data. Since this observation has been made repeatedly, it seems typical for dynamics in NLC. However, the reasons for the difference between the NLC spectrum and the Nastrom-Gage spectrum are not understood yet.

5.3 Simultaneous Camera and Lidar Observations

There are in total three events from the years 2014 and 2015 with simultaneous NLC detection by the camera in Trondheim and the ALOMAR RMR lidar.

July 23, 2014

The first case on July 23, 2014, is shown in Fig. 5.7. The horizontal map exposes several parallel bands aligned in north-northeast to south-southwestern direction and an extend of several hundred kilometers (Fig. 5.8). The lidar beams were tilted 20° off-zenith in northern respectively eastern direction, their positions in the images are shown in Fig. 5.7. Both lidar timeseries show strong and sudden vertical displacements of the NLC layer in regular time intervals of 20 - 30 minutes (Fig. 5.9). The time series of brightness as seen by camera at the lidar sounding volume is shown in Fig. 5.10. Due to ISO jumps occurring variations of the brightness are shown as described in 4.2.2.

The relevant area of the picture is quite bright making it hard to resolve structured NLC directly in time series. Both the high solar elevation angle in the end of July and

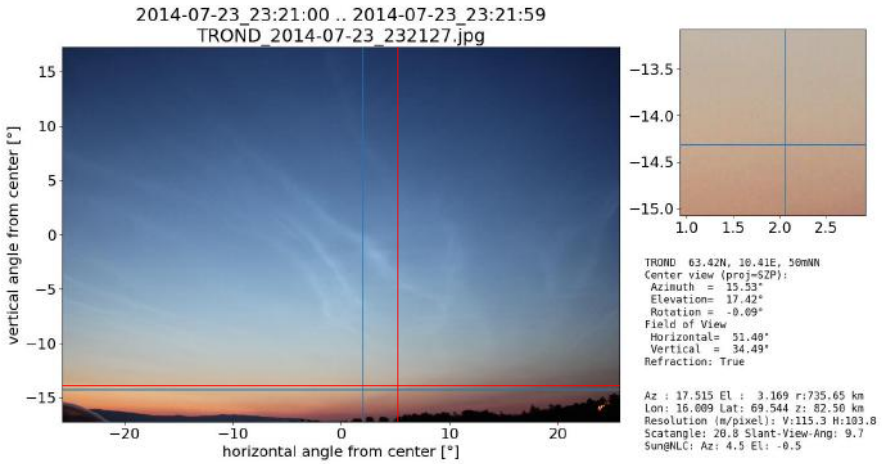

Figure 5.7: NLC display seen from Trondheim on July 23, 2014, 23:21:27 UT: The blue and red cross indicate the position of the beam of the ALOMAR RMR lidar at an altitude of 83 km. The blue cross corresponds to the NWT, the red one to the SET.

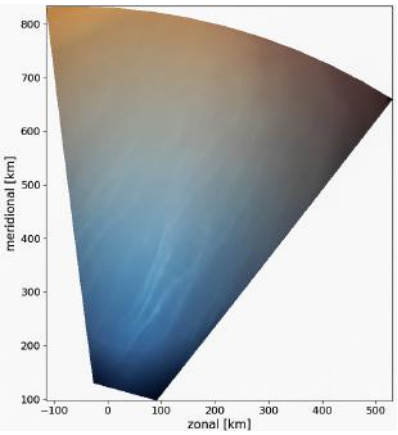

Figure 5.8: Horizontal map of the NLC display on July 23, 2014, at 23:21:27 UT.

the fact that the NLC is of type III with a large vertical extend and complex structures, weakens the contrast of structures that are identified as NLC in the camera images. This can be seen in the upper two panels of Fig. 5.10 where the brightness series of the pixels associated with the lidar is nearly completely following the solar elevation angle having its minimum around local midnight (ca. 23 UT). For the SET a small brightness increase is observed around 23:20 at the time of minimum solar elevation that may be linked to the enhanced brightness seen by the lidar at this time. Also time series from a point in the middle of the image are extracted where the contrast of NLC structures is higher. At this point the scattering angle is 29.0° and the slant-view angle is 19.6° (as compared to 20.8° (NWT) respectively 23.7° (SET) and 9.7° respectively 9.8° at the points above ALOMAR). In the lower panel of Fig. 5.10 clear brightness peaks in a regular separation are visible. The separation is 10-15 minutes which is half of the

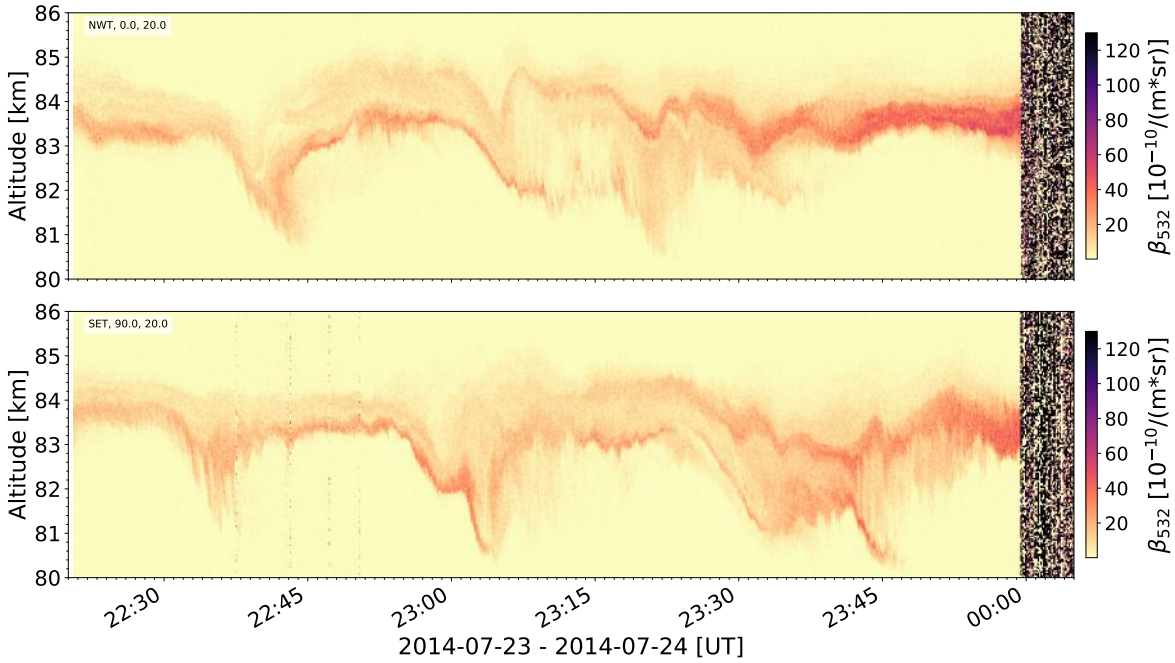

Figure 5.9: LISA profile from North-West and South-East telescope from July 23-24, 2014, 22:20:00 - 00:05:00 UT.

separation of the altitude drops in the lidar data shown in Fig. 5.9. Due to the spatial separation of the measurement volumes no conclusion about a correlation between the brightness in the camera time series and the altitude drops in the lidar profiles is possible. However, if these two characteristics were linked to the same structure in the NLC, these observations would indicate longer horizontal wavelengths at higher latitudes during this event.

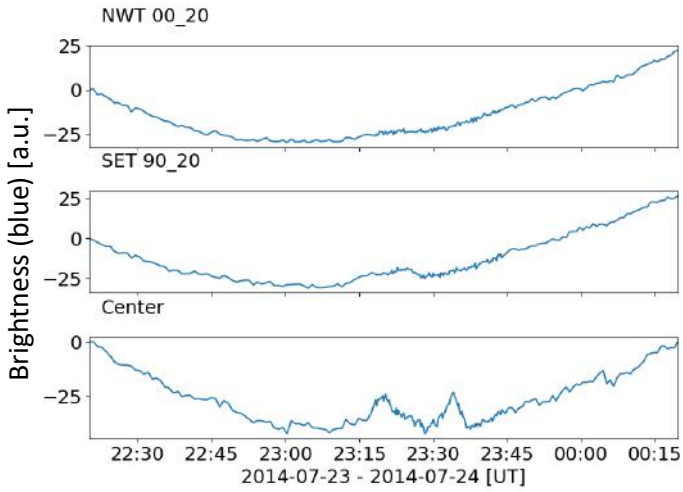

Figure 5.10: Brightness time series from July 23-24, 2014, at the positions of the North-West and the South-East telescope and the center of the image, corresponding to 65.542°N, 11.837°E in 83 km altitude.

August 15-16, 2015

The second event is on August 15, 2015. The NLC display in the camera image was much closer to the horizon than in the previous case. This involves a more favorable illumination of the relevant part of the image where the lidar measured the clouds. Also the ISO speed of the camera is constant in the relevant time period from 21:50 to 00:40 UT. Both lidar telescopes were oriented towards the zenith during this night. The NLC display and the point of view of the ALOMAR telescopes are shown in Fig. 5.11. For comparison the NLC backscatter coefficient and the particle size and density distribution at the same time are plotted besides. The particle size information is integrated in 2-minute intervals.

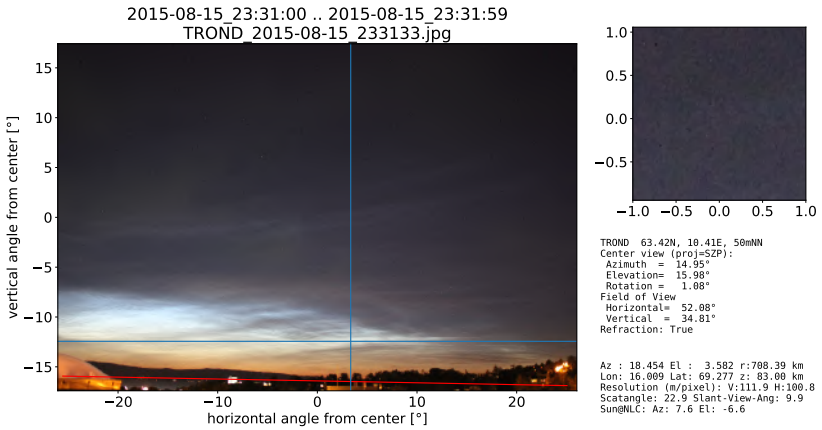

Figure 5.11: NLC display seen from Trondheim on August 15, 2015: The blue cross indicates the position of the beams of the ALOMAR RMR lidar at an altitude of 83 km.

The scattering angle ranges from 37.0° at 22:20 to 19.8° at 23:50 UT. According to the $(1 + \cos^2(\gamma))$ dependency of the Rayleigh backscatter the backscattered intensity decreases by 13.1% during this time. To interpret this value an estimation is necessary to which extent the pixel brightness is impacted by NLC at all. Another date is chosen for this because the end of NLC observation in the relevant volume coincides with thin tropospheric clouds entering the camera image on the current date and a clear distinction between decreasing NLC and increasing tropospheric clouds is difficult. On July 23, 2014, at about 23:20 UT the difference in the blue brightness value between the presence of an NLC band and no NLC is better to read (see Fig. 5.10) and is determined as 20 (in the presence of a scattering angle of 27.3° that is mid in the before mentioned range from 19.8° to 37.0°). Assuming this value a decrease in Rayleigh

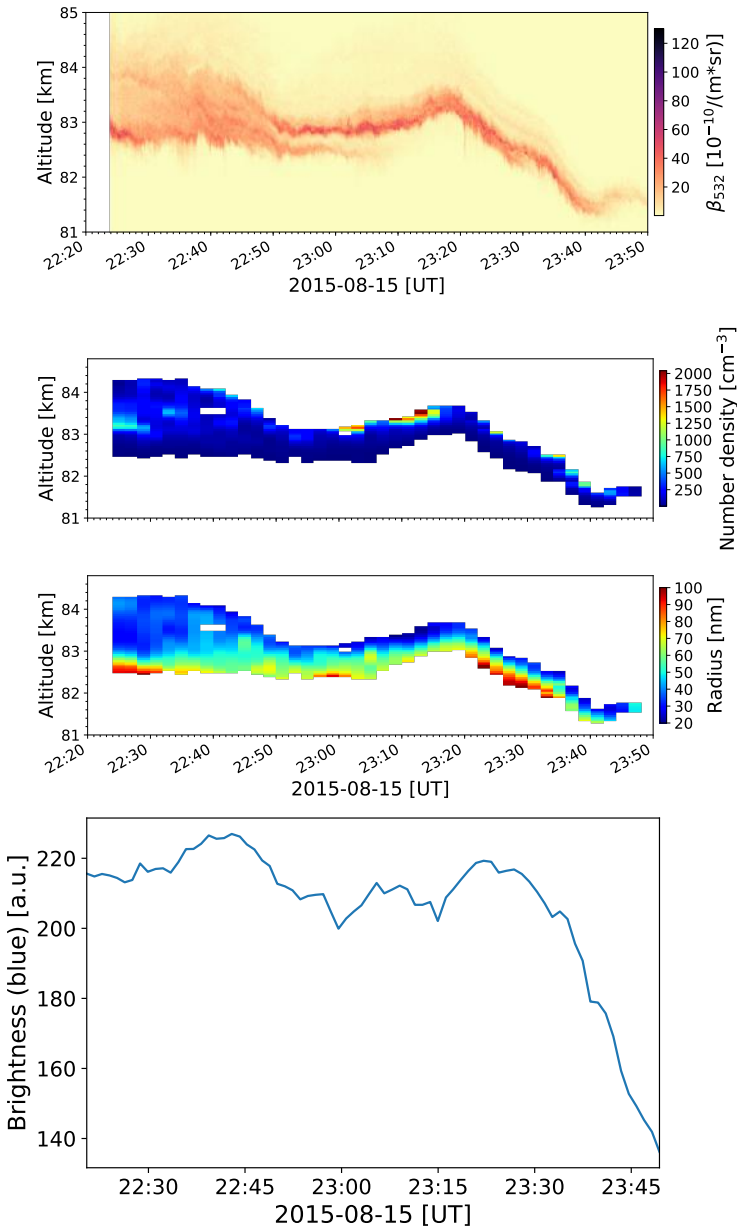

Figure 5.12: Analysis of brightness from Trondheim camera as well as backscatter and particle size from ALOMAR lidar on August 15, 2015, 22:20 - 23:50 UT:
Upper panel: NLC backscatter coefficient averaged for North-West and South-East telescope since both were pointing towards the zenith.
Middle panel: Particle radii and number density of particles averaged for the North-West and South-East telescope.
Lower panel: Brightness time series extracted from camera images.

backscatter intensity of 13 % implicates a decrease of the pixel brightness of 2.6. This is small compared to the variations visible in the time series.

The end of the time period shown in Fig. 5.12 is analyzed in detail in Fig. 5.13. Until 23:30 UT no disturbance of the brightness by tropospheric clouds occurs, afterward

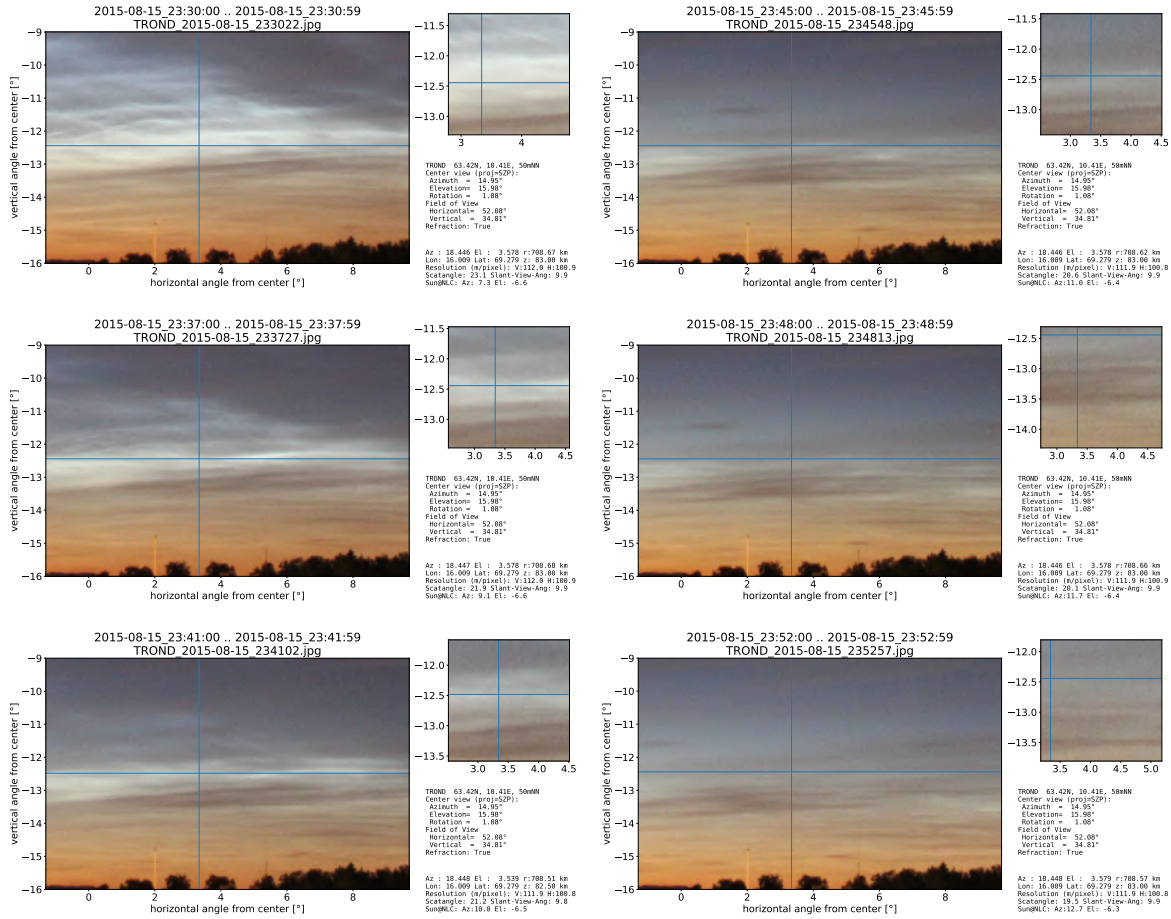

Figure 5.13: NLC volume observed by lidar (blue cross) seen in camera images at 23:30:22, 23:37:27, 23:41:02, 23:45:48, 23:48:13 and 23:52:57 UT.

some clouds form at low elevation angles. The blue cross indicating the ALOMAR lidar's position is above the area with tropospheric clouds until 23:45 and also the thinner gray stripe developing at that time at about 12° elevation only borders the measurement volume slightly in the following. Nevertheless, it might contribute to the strong decrease in pixel brightness after 23:40 UT. From the analogy of brightness time series and particle radius a correlation between a bigger particle radius and higher brightness is observed. Also a larger thickness of the layer increases the visibility when the particles are of sufficient size. It is observed that in the time of the brightness decrease the particle size drops from 100 nm to 40 nm. According to equation 2.1 this corresponds to a brightness decrease of 99.6 %. So the decrease seen is in fact caused by the changes in the NLC. It is found that a size of 50-60 nm is needed to identify NLC in this case.

August 16-17, 2015

The third event with simultaneous camera and lidar observation is on August 16-17, 2015. The NLC detected by the lidar was much fainter than during the other two events and is shown in Fig. 5.15. The backscatter coefficient was only $15 \cdot 10^{-10}/(\mathrm{m} \cdot \mathrm{sr})$ compared to a maximum of $80 \cdot 10^{-10}/(\mathrm{m} \cdot \mathrm{sr})$ on August 15, 2015, combined with very thin layers. In the camera images an unstructured NLC is seen in the relevant pixels as shown in Fig. 5.14. Structured NLC were located further west and ant higher elevation angles. In the brightness time series given in Fig. 5.16 a uniform increase is observed from 23:10 until 23:58 UT which is larger than the decrease before the minimum at 23:00 UT. At 23:58 UT the brightness reaches a peak, then drops slightly and increases again from 00:11 on due to the increasing solar elevation. Since the increase in brightness in the camera time series starts earlier than the NLC detection in the lidar and the lidar is the more sensitive instrument this effect may not only be assigned to NLC but also to the appearance of aurora borealis at the time from 23:30 to 00:00 UT. Aurora boraelis occurred in all parts of the image. These conditions together with the NLC appearing in the lidar first about one hour after local midnight make any further detailed analysis impossible in this case.

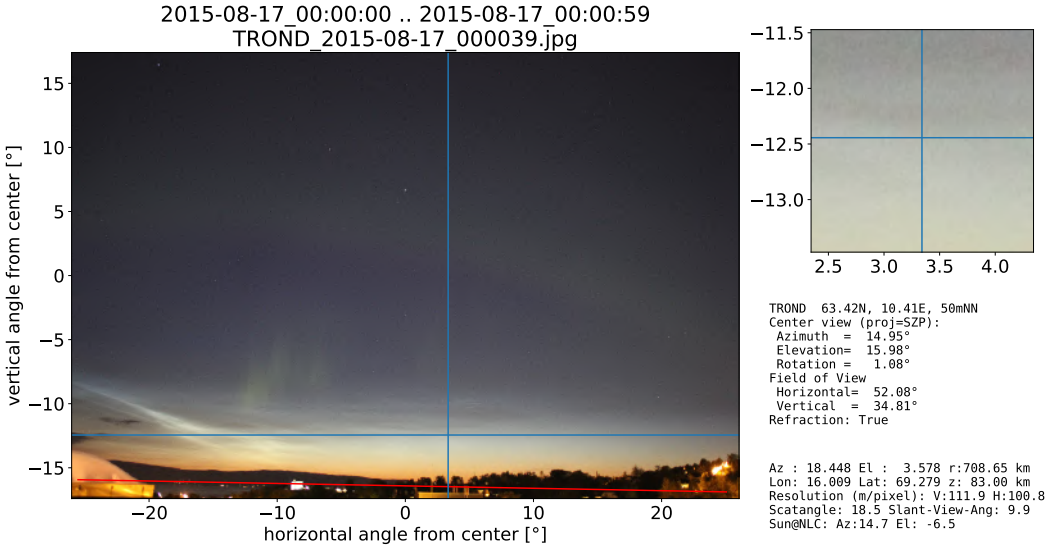

Figure 5.14: NLC display from August 17, 2015, 00:00:39 UT: The blue cross indicates the position of the lidar beams.

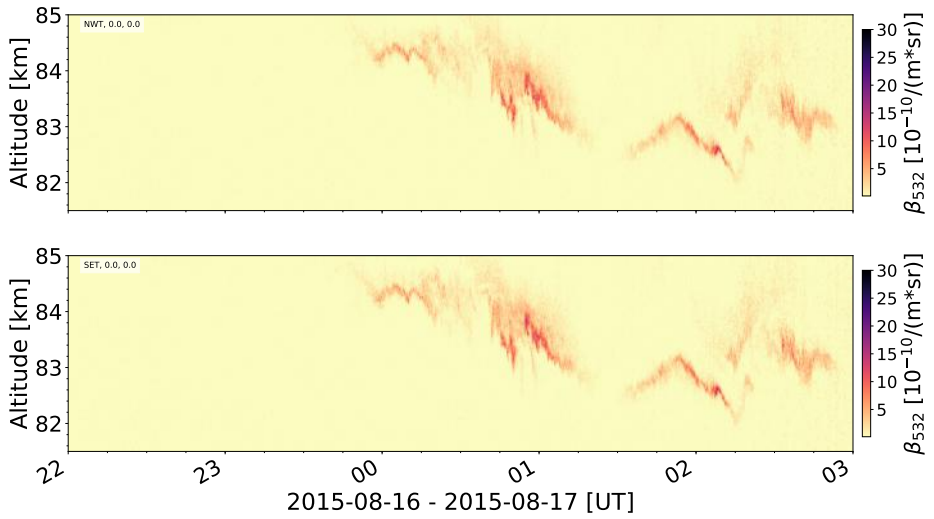

Figure 5.15: Lidar profile from August 16-17, 2015: Note the different color scaling compared to other events.

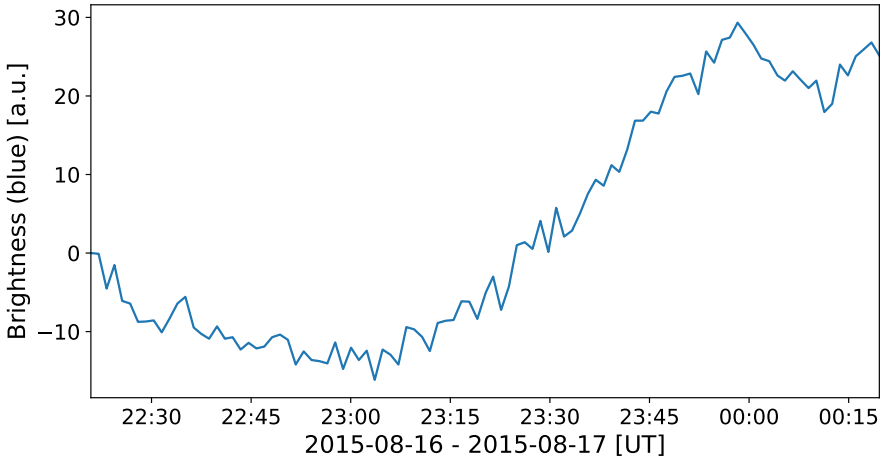

Figure 5.16: Brightness time series from camera images on August 16-17, 2015, 22:20 - 00:20 UT.

Summarizing, three cases of simultaneous NLC observations by lidar and camera were analyzed including different NLC types. Different influences on the brightness of pixels like scattering angle, particle size and other effects like polar lights are discussed. The particle size is found to have the strongest impact on the pixel brightness and a correlation between particle size and visibility in camera images is found.

Chapter 6

Conclusions and Outlook

Summary

This thesis addresses small-scale features in noctilucent clouds using camera and lidar data, applying different techniques such as categorization and occurrence statistics, spectral analysis and pooling of data from different instruments. For the first time NLC backscatter coefficients from the lidar single-shot acquisition software LISA are processed. With this high time resolution even smaller wave structures were found than previously expected. Especially in cases where the data with 30 s temporal resolution looks discontinuous, in the data with 1 s resolution waves are found. According to the novel structures found, new categories were defined. A statistical evaluation of the occurrence of theses types is done for the summer 2014, wave periods under 5 minutes are observed at more than half of the total NLC measurement duration in both thin and thick layers. In a spectral analysis the existence of wave structures could be proven down to scales from 10 minutes to 10 s. Applying a simple advection model with a horizontal wind speed of 40 m/s, LISA resolves wave structures from 400 m to 24 km by that. A common average slope is found to be -2.0. A spectral analysis was also performed for high-resolution images of NLC. Here the same slope of -2.0 was found. Finally, three events with a simultaneous detection of the same NLC by camera and lidar were discussed. In one case a comparison between brightness in camera images, brightness in lidar backscatter and particle size measured by three-color lidar is used to determine sufficient particle sizes for the detection of NLC by cameras. A radius of 50-60 nm is found for that.

Outlook

There are many ideas that can further be applied to high-resolution NLC data in order to extend the existing knowledge about small-scale gravity waves and instabilities.

One relevant topic are winds. Despite the small scales being analyzed, at some points rather rough approximations for horizontal winds had to be made or winds were simply ignored. One promising technique to introduce a more accurate way of treating winds in image data of NLC is the optical flow. By detecting image objects in a picture and recognizing them in a later one motion vectors can be extracted. The algorithm calculates a 2D vector field of apparent motions of image objects between two consecutive frames (Kanade). This method is commonly used in many applications of image and video processing for motion detection and estimation but also for video compression and stabilization.

Concerning the simultaneous observation of NLC by lidar and camera valuable results were obtained, but further detections of high quality and higher resolution by the cameras are desirable. There are strong limitations for recording simultaneous data such as the limited number of days that in principle accounts for camera observations from Trondheim due the high solar elevation earlier in the season. Another important factor with impact on data quality is the distance between lidar and camera. For smaller distances the elevation angle of the relevant pixels in image data would be larger, implicating a higher resolution per pixel and less uncertainties due to refraction. On the other hand, installing a camera closer to the ALOMAR lidar would implicate that it is placed further north and even fewer days of NLC detection are possible due to the polar summer. In conclusion, the choice of exposure time, aperture value and ISO speed might still be optimized and extended with high-dynamic range imaging to illuminate the relevant areas of the image and the whole field of view of the camera properly.

Concerning the newly defined categories, an investigation of their occurrence depending on other variables like altitude, absolute value of backscatter coefficient or day of the year/season could be performed. More seasons should be analyzed in order to determine year-to-year variations. Also, spectral analysis should be extended to more events in order to give evidence if the slope of -2.0 is typical for NLC. An automation of the categorization is desirable in order to analyze the data of more years in shorter intervals with less effort and higher objectivity.

Bibliography

T. W. Backhouse. The luminous cirrus clouds of june and july. *Meteorol. Mag.*, 20:133, Sept. 1885.

G. Baumgarten. Doppler Rayleigh/Mie/Raman lidar for wind and temperature measurements in the middle atmosphere up to 80 km. *Atmospheric Measurement Techniques*, 3(6):1509–1518, 2010. doi: 10.5194/amt-3-1509-2010. URL https://www.atmos-meas-tech.net/3/1509/2010/.

G. Baumgarten and D. C. Fritts. Quantifying Kelvin-Helmholtz instability dynamics observed in noctilucent clouds: 1. Methods and observations. *Journal of Geophysical Research: Atmospheres*, 119(15):9324–9337, 2014.

G. Baumgarten, J. Fiedler, and G. von Cossart. The size of noctilucent cloud particles above ALOMAR (69N,16E): Optical modeling and method description. *Advances in Space Research*, 40(6):772 – 784, 2007. ISSN 0273-1177. doi: https://doi.org/10.1016/j.asr.2007.01.018. URL http://www.sciencedirect.com/science/article/pii/S0273117707000178.

B. A. Bodhaine, N. B. Wood, E. G. Dutton, and J. R. Slusser. On rayleigh optical depth calculations. *Journal of Atmospheric and Oceanic Technology*, 16(11):1854–1861, 1999. doi: 10.1175/1520-0426(1999)016<1854:ORODC>2.0.CO;2. URL https://doi.org/10.1175/1520-0426(1999)016<1854:ORODC>2.0.CO;2.

J. Fiedler, G. Baumgarten, U. Berger, P. Hoffmann, N. Kaifler, and F.-J. Lübken. NLC and the background atmosphere above ALOMAR. *Atmospheric Chemistry and Physics*, 11(12):5701–5717, 2011. doi: 10.5194/acp-11-5701-2011. URL https://www.atmos-chem-phys.net/11/5701/2011/.

J. Fiedler, G. Baumgarten, U. Berger, and F.-J. Lübken. Long-term variations of noctilucent clouds at ALOMAR. *Journal of Atmospheric and Solar-Terrestrial Physics*, 162:79–89, Sept. 2017. doi: 10.1016/j.jastp.2016.08.006.

B. Fogle and B. Haurwitz. *Noctilucent Clouds*, volume 6. Space Sci Rev, 1966. doi: https://doi.org/10.1007/BF00173768.

D. C. Fritts, L. Wang, G. Baumgarten, A. D. Miller, M. A. Geller, G. Jones, M. Limon, D. Chapman, J. Didier, C. B. Kjellstrand, D. Araujo, S. Hillbrand, A. Korotkov, G. Tucker, and J. Vinokurov. High-resolution observations and modeling of turbulence sources, structures, and intensities in the upper mesosphere. *Journal of Atmospheric and Solar-Terrestrial Physics*, 162:57 – 78, 2017. ISSN 1364-6826. doi: https://doi.org/10.1016/j.jastp.2016.11.006. URL http://www.sciencedirect.com/science/article/pii/S1364682616304126. Layered Phenomena in the Mesopause Region.

Description of ALOMAR RMR lidar on IAP website. IAP. URL https://www.iap-kborn.de/forschung/abteilung-optische-sondierungen-und-hoehenforschungsraketen/instrumente-und-modelle/alomar-rmr-lidar.

Parameter values for the HDTV standards for production and international programme exchange, number 6 in 709, 2015. ITU-R, International Telecommunication Union, Radiocommunication. URL https://www.itu.int/dms_pubrec/itu-r/rec/bt/R-REC-BT.709-6-201506-I!!PDF-E.pdf.

O. Jesse. Auffallende Abenderscheinungen am Himmel. *Meteorologische Zeitschrift*, 2: 311–312, Aug. 1885.

O. Jesse. Die Höhe der leuchtenden Nachtwolken. *Astronomische Nachrichten*, 1896.

N. Kaifler. Quantification of waves in lidar observations of noctilucent clouds at scales from seconds to minutes. *Atmos. Chem. Phys., 13, 11757–11768*, 2013. doi: doi:10.5194/acp-13-11757-2013.

L. Kanade. Optical Flow OpenCV Tutorial. URL https://www.docs.opencv.org/trunk/d7/d8b/tutorial_py_lucas_kanade.html.

J. Kiliani, G. Baumgarten, F.-J. Lübken, U. Berger, and P. Hoffmann. Temporal and spatial characteristics of the formation of strong noctilucent clouds. *Journal of Atmospheric and Solar-Terrestrial Physics*, 104:151–166, 2013.

A. A. Kokhanovsky. *Optics of Light Scattering Media*. Springer Verlag, 2001. ISBN 1-85233-404-5.

M. R. Kondabathula. Camera Based Detection and Localization of Noctilucent Clouds, 2018.

F.-J. Lübken. Thermal structure of the arctic summer mesosphere. *Journal of Geophysical Research: Atmospheres*, 104(D8):9135–9149, 1999. doi: 10.1029/1999JD900076. URL https://agupubs.onlinelibrary.wiley.com/doi/abs/10.1029/1999JD900076.

R. C. Leslie. Sky glows. *Nature*, 32:245, July 1885. URL https://doi.org/10.1038/032245a0.

R. S. Lindzen. Turbulence and stress owing to gravity wave and tidal breakdown. *Journal of Geophysical Research: Oceans*, 86(C10):9707–9714, 1981. doi: 10.1029/JC086iC10p09707. URL https://agupubs.onlinelibrary.wiley.com/doi/abs/10.1029/JC086iC10p09707.

F.-J. Lübken, U. Berger, and G. Baumgarten. On the anthropogenic impact on long-term evolution of noctilucent clouds. *Geophysical Research Letters*, 2018. doi: https://doi.org/10.1029/2018GL077719.

G. D. Nastrom and K. S. Gage. A climatology of atmospheric wavenumber spectra of wind and temperature observed by commercial aircraft. *Journal of the Atmospheric Sciences*, 42(9):950–960, 1985. doi: 10.1175/1520-0469(1985)042<0950:ACOAWS>2.0.CO;2. URL https://doi.org/10.1175/1520-0469(1985)042<0950:ACOAWS>2.0.CO;2.

V. Nussbaumer, K. H. Fricke, M. Langer, W. Singer, and U. von Zahn. First simultaneous and common volume observations of noctilucent clouds and polar mesosphere summer echoes by lidar and radar. *Journal of Geophysical Research: Atmospheres*, 101(D14):19161–19167, 1996. doi: 10.1029/96JD01213. URL https://agupubs.onlinelibrary.wiley.com/doi/abs/10.1029/96JD01213.

J. M. Picone, A. E. Hedin, D. P. Drob, and A. C. Aikin. NRLMSISE-00 empirical model of the atmosphere: Statistical comparisons and scientific issues. *Journal of Geophysical Research: Space Physics*, 107(A12):SIA 15–1–SIA 15–16, 2002. doi: 10.1029/2002JA009430. URL https://agupubs.onlinelibrary.wiley.com/doi/abs/10.1029/2002JA009430.

PIL. Python image library. URL http://www.pythonware.com/products/pil/.

proj4. Python package proj. URL https://proj4.org/.

C. Ridder, G. Baumgarten, J. Fiedler, F.-J. Lübken, and G. Stober. Analysis of small-scale structures in lidar observations of noctilucent clouds using a pattern recognition method. *Journal of Atmospheric and Solar-Terrestrial Physics*, 162:48 – 56, 2017. ISSN 1364-6826. doi: https://doi.org/10.1016/j.jastp.2017.04.005. URL http://www.sciencedirect.com/science/article/pii/S1364682617302535. Layered Phenomena in the Mesopause Region.

J. M. Russell, S. M. Bailey, L. L. Gordley, D. W. Rusch, M. Horányi, M. E. Hervig, G. E. Thomas, C. E. Randall, D. E. Siskind, M. H. Stevens, et al. The Aeronomy of Ice in the Mesosphere (AIM) mission: Overview and early science results. *Journal of Atmospheric and Solar-Terrestrial Physics*, 71(3):289–299, 2009.

B. Schäfer. Bestimmung von Höhe und horizontaler Struktur leuchtender Nachtwolken (NLC) aus Kamerabildern durch Triangulation, 2016. URL https://www.iap-kborn.de/fileadmin/user_upload/MAIN-abteilung/optik/Forschung/Bachelor/Schaefer-Bachelor-2015.pdf.

D. Schmidt. Automatische Erkennung von leuchtenden Nachtwolken in Kamerabeobachtungen, 2013. URL https://www.iap-kborn.de/fileadmin/user_upload/MAIN-abteilung/optik/Forschung/Bachelor/Schmidt-Bachelor-2013.pdf.

G. E. Thomas, J. J. Olivero, E. J. Jensen, W. Schroeder, and O. B. Toon. Relation between increasing methane and the presence of ice clouds at the mesopause. , 338:490–492, Apr. 1989. doi: 10.1038/338490a0.

G. von Cossart, J. Fiedler, and U. von Zahn. Size distributions of NLC particles as determined from 3-color observations of NLC by ground-based lidar. *Geophysical Research Letters*, 26(11):1513–1516, 1999. doi: 10.1029/1999GL900226. URL https://agupubs.onlinelibrary.wiley.com/doi/abs/10.1029/1999GL900226.

U. von Zahn, G. von Cossart, J. Fiedler, K. H. Fricke, G. Nelke, G. Baumgarten, D. Rees, A. Hauchecorne, and K. Adolfsen. The ALOMAR Rayleigh/Mie/Raman lidar: objectives, configuration, and performance. *Annales Geophysicae*, 18:815–833, July 2000. doi: 10.1007/s00585-000-0815-2.

P. D. Welch. The Use of Fast Fourier Transform for the Estimation of Power Spectra: A Method Based on Time Aver. aging Over Short, Modified Periodograms. *IEEE Transactions on Audio and Electroacoustics*, 15(2):70–73, 1967.

WGS. *World Geodetic System 1984*. National Imagery and Mapping Agency: Department of Defense.

A. Y. Zasetsky, S. V. Petelina, R. Remorov, C. D. Boone, P. F. Bernath, and E. J. Llewellyn. Ice particle growth in the polar summer mesosphere: Formation time and equilibrium size. *Geophysical Research Letters*, 36(15):n/a–n/a, 2009. ISSN 1944-8007. doi: 10.1029/2009GL038727. URL http://dx.doi.org/10.1029/2009GL038727. L15803.

Acknowledgments

I am grateful to my first supervisor Prof. Dr. Franz-Josef Lübken for offering me to write my master thesis at IAP and his ideas on my topic. Next I would like to thank Dr. Gerd Baumgarten for his valuable comments on my work and helping me with programming issues. I also want to thank everyone contributing to the long time series of lidar measurements at ALOMAR including IAP staff, the Norwegian ALOMAR staff and measuring students. I am grateful for the opportunity to take part in these measurements a number of times as well.

Further I wish to thank my family for always supporting my in my projects and studies. Last but not least I would like to thank my bicycle for never having had a flat tire or other issues during my period at IAP and always carrying me safely on the 27 km long way between the institute and home in all weather conditions.

Selbstständigkeitserklärung

Ich versichere hiermit an Eides statt, dass ich die vorliegende Arbeit selbstständig angefertigt und ohne fremde Hilfe verfasst habe, keine außer den von mir angegebenen Hilfsmitteln und Quellen dazu verwendet habe und die den benutzten Werken inhaltlich und wörtlich entnommenen Stellen als solche kenntlich gemacht habe.

Rostock, 22. März 2019